ANL-79-23

332
7-25-79

MASTER

ANL-79-23

DR. 2896

MATERIALS TECHNOLOGY FOR COAL-CONVERSION PROCESSES

Sixteenth Quarterly Report

October—December 1978

U of C-AUA-USDOE

ARGONNE NATIONAL LABORATORY, ARGONNE, ILLINOIS

Prepared for the Office of Fossil Energy,
U. S. DEPARTMENT OF ENERGY
under Contract W-31-109-Eng-38

DISCLAIMER

The facilities of Argonne National Laboratory are owned by the United States Government. Under the terms of a contract (W-31-109-Eng-38) among the U. S. Department of Energy, Argonne Universities Association and The University of Chicago, the University employs the staff and operates the Laboratory in accordance with policies and programs formulated, approved and reviewed by the Association.

MEMBERS OF ARGONNE UNIVERSITIES ASSOCIATION

The University of Arizona
Carnegie-Mellon University
Case Western Reserve University
The University of Chicago
University of Cincinnati
Illinois Institute of Technology
University of Illinois
Indiana University
The University of Iowa
Iowa State University
The University of Kansas
Kansas State University
Loyola University of Chicago
Marquette University
The University of Michigan
Michigan State University
University of Minnesota
University of Missouri
Northwestern University
University of Notre Dame
The Ohio State University
Ohio University
The Pennsylvania State University
Purdue University
Saint Louis University
Southern Illinois University
The University of Texas at Austin
Washington University
Wayne State University
The University of Wisconsin-Madison

NOTICE

This report was prepared as an account of work sponsored by the United States Government. Neither the United States nor the United States Department of Energy, nor any of their employees, nor any of their contractors, subcontractors, or their employees, makes any warranty, express or implied, or assumes any legal liability or responsibility for the accuracy, completeness or usefulness of any information, apparatus, product or process disclosed, or represents that its use would not infringe privately-owned rights. Mention of commercial products, their manufacturers, or their suppliers in this publication does not imply or connote approval or disapproval of the product by Argonne National Laboratory or the U. S. Department of Energy.

Printed in the United States of America
Available from
National Technical Information Service
U. S. Department of Commerce
5285 Port Royal Road
Springfield, Virginia 22161
Price: Printed Copy $6.00; Microfiche $3.00

Distribution Categories:
Coal Conversion and Utilization:
Coal Gasification (UC-90c)
Direct Combustion of Coal (UC-90e)
Materials and Components (UC-90h)

ANL-79-23

ARGONNE NATIONAL LABORATORY
9700 South Cass Avenue
Argonne, Illinois 60439

MATERIALS TECHNOLOGY FOR COAL-CONVERSION PROCESSES

Sixteenth Quarterly Report
October—December 1978

W. A. Ellingson
Project Leader

Materials Science Division

Most recent reports in this series

ANL-78-6	July—December 1977
ANL-78-54	January—March 1978
ANL-78-79	April—June 1978
ANL-79-2	July—September 1978

THIS PAGE

WAS INTENTIONALLY

LEFT BLANK

TABLE OF CONTENTS

TABLE OF CONTENTS (continued)

LIST OF FIGURES

LIST OF FIGURES (contd.)

LIST OF FIGURES (contd.)

LIST OF TABLES

MATERIALS TECHNOLOGY FOR COAL-CONVERSION PROCESSES: SIXTEENTH QUARTERLY REPORT

October-December 1978

HIGHLIGHTS

Task A -- Evaluation of Ceramic Refractories for Slagging Gasifiers

(C.R. Kennedy, S.W. Kreis, and R.J. Fousek)

The slag from test run 8 has been analyzed and was found to have a base-to-acid ratio of 0.7 and a ferritic content of 15-18%.

Test runs 10 and 11 have been completed and the results are being compiled and analyzed.

Samples of slag have been obtained from slagging gasifiers at Grand Forks Energy Research Center and Combustion Engineering. Analysis of this slag reveals ferritic contents of 18-61%, indicating that the partial pressure of oxygen in the slagging zone is $\sim 10^{-2}$ to 10^{-4} Pa.

Task C -- Application and Development of Nondestructive Evaluation Methods for Coal-conversion Processes

(W.A. Ellingson, K.J. Reimann, W.J. Shack, and C.A. Youngdahl)

A second automatic-mode field test of the high-temperature erosion-monitoring system was completed at the Bi-Gas pilot plant. Data were obtained from Type 304 stainless steel. Present results suggest that reliable thickness values have been obtained. The HYGAS cyclone separator was again monitored ultrasonically for erosive wear after about 5000 h of service. The wear rate appears to have been reduced in the stellite region as the result of changes in the methods of coal preparation and cyclone operation.

The acoustic leak-detection system for detecting internal gas leakage past ball valves in coal-feed systems was field tested at the Morgantown Energy Technology Center. A 150-mm-diameter valve was tested at room temperature through a range of pressures from 0.34 to 4.05 MPa. Present results suggest a direct rms relation to measured leak rates.

Work on the detection of acoustic emission from thermally excited refractory concrete continued with the development of real-time data-acquisition systems using digital computers.

Field visits to H-Coal, EXXON and CRESAP pilot liquefaction facilities were made to discuss application of NDE methods developed for gasification plants.

Task D.1 -- Corrosion in Gasification Environments *(K. Natesan)*

Uniaxial tensile data were generated for Incoloy 800, Type 310 stainless steel, Inconel 671, and U.S. Steel Alloy 18-18-2 in the as-received and thermally aged conditions and after 3.6-Ms exposures to multicomponent gas mixtures that simulate a coal-gasification environment. The preexposure of the materials to complex gas mixtures resulted in a decrease in ultimate tensile strength and flow stress of the material when compared to those of as-received and thermally aged specimens.

Experimental results on the corrosion behavior of Type 310 stainless steel and Incoloy 800 in multicomponent gas environments clearly showed that for a given sulfur partial pressure, there exists a threshold in oxygen partial pressure above which a continuous protective oxide scale is developed on the specimens. This threshold oxygen partial pressure is $\sim 10^3$ times the oxygen partial pressure for the Cr oxide/Cr sulfide equilibrium.

Task D.2 -- Effect of Sulfation Accelerators and Corrosion Inhibitors on Materials in Fluidized-bed Combustion Systems *(O.K. Chopra)*

The corrosion behavior of several commercial iron- and nickel-base alloys has been evaluated after 100-h exposures in the bed and freeboard regions of an atmospheric-pressure fluidized-bed combustor. The influence of small additions of NaCl and $CaCl_2$ (i.e., sulfation-enhancement agents) to the limestone on the average thickness of the surface scale and internal corrosive penetration at temperatures between $\sim$ 430 and 845°C was determined from metallographic evaluation of the specimens. The results showed that the addition of 0.3 mole % $CaCl_2$ to the fluidized bed had no effect on the corrosion behavior of the various materials; however, 0.5 mole % NaCl increased the corrosion rate of all materials. In the presence of NaCl, austenitic stainless steels and Haynes alloy 188 exhibited better corrosion resistance than the high-nickel alloys, although Hastelloy-X, Inconel 625, and Inconel 718 also showed good resistance against accelerated corrosion of plant materials.

Task E -- Erosion Behavior of Materials in Coal-conversion Processes *(J.Y. Park, S. Danyluk, and W.J. Shack)*

High-temperature corrosion calibration tests were attempted in an MPC-selected corrosion test atmosphere at atmospheric pressure and 816°C. The tests, however, were interrupted because of a cooling-water leak which caused a flood in the test chamber. The test apparatus is being repaired, and an improved safety shutoff system installed.

Task F -- Component Performance and Failure Analysis *(S. Danyluk, G.M. Dragel and L.E. Pahis)*

The highlights of the work accomplished in the previous quarter may be summarized as follows: (1) The design and assembly of thermowells

(Haynes Alloy 188 and slurry-coated Type 310 stainless steel) has been initiated and the necessary material has been procured. (2) Components from the Synthane boiler explosion have been examined. The specific mechanical/materials malfunction which led to the explosion could not be identified. (3) Cracks in steam piping from the IGT Steam-Iron Pilot Plant were examined. (4) A cracked pump shaft and embrittled heat-exchanger tube from the HYGAS Pilot Plant were examined. (5) The erosion of a carbon steel pipe from the Westinghouse Coal Gasification PDU was examined.

MATERIALS TECHNOLOGY FOR COAL-CONVERSION PROCESSES:
SIXTEENTH QUARTERLY REPORT,
October-December 1978

FOREWORD

This broad-base materials engineering program, begun in 1974, includes studies on ceramic (refractory) and metallic materials presently being used or intended for use in coal-conversion processes. The program entails nondestructive testing, failure analysis, and studies of erosive wear, corrosion and refractory degradation. Appropriate laboratory and field experiments are integrated such that the results have impact on present pilot- and demonstration-plant and proposed full-scale designs. This quarterly report, for the period October-December 1978, presents the technical accomplishments of the program.

ABSTRACT

Refractories for slag containment, nondestructive evaluation methods, corrosion, erosion, and component failures were studied.

Analysis of coal slags from Grand Forks Energy Technology Center and Combustion Engineering reveal ferritic contents of 18-61%, suggesting a partial pressure of O_2 in the slagging zone of $\sim 10^{-2}$ to 10^{-4} Pa.

A second field test of the high-temperature ultrasonic erosion-monitoring system was completed. Ultrasonic inspection of the HYGAS cyclone separator shows a reduced erosive-wear rate at 5000 h in the stellite region.

The acoustic leak-detection system for valves was field tested at the Morgantown Energy Technology Center using a 150-mm-dia. valve with a range of pressures from 0.34 to 4.05 MPa. Results suggest a linear relation between detected rms levels and leak rates. Studies on acoustic emissions from refractory concrete continued with further development of a real-time data acquisition system.

Corrosion studies were conducted on Incoloy 800, Type 310 stainless steel, Inconel 671 and U.S. Steel Alloy 18-18-2 (as-received, thermally aged, and preexposed for 3.6 Ms to multicomponent gas mixtures). Results suggest a decrease in ultimate tensile strength and flow stress after preexposure.

Examination of commercial iron- and nickel-base alloys after 100-h exposures in atmospheric-pressure fluidized-bed combustors suggests that the addition of 0.3 mole % $CaCl_2$ to the fluidized bed has no effect on the corrosion behavior of these materials; however, 0.5 mole % NaCl increased the corrosion rate of all materials.

Failure-analysis activities included (1) the design and assembly of thermowells (Haynes Alloy 188 and slurry-coated Type 310 stainless steel) and (2) examination of components from the Synthane boiler explosion, the IGT Steam-Iron Pilot Plant, the HYGAS Ash Agglomerating Gasifier, and the Westinghouse Coal Gasification PDU.

INTRODUCTION

The economical conversion of coal into clean and usable fuels will be advanced through the use of durable materials systems. The technical information base applicable to materials selection in plant design for the operating environments of various coal-conversion processes is extremely limited. Hence, reliable selection and lifetime-prediction methods for materials under these conditions are not available. This project is designed to provide part of the materials information necessary for successful operation of coal-conversion systems. The present report is the sixteenth quarterly progress report submitted by ANL to the Division of Systems Engineering, Office of Fossil Energy under Project Number 7106, "Materials Technology for Coal-conversion Processes".

The project includes six tasks: (A) evaluation of commercial refractories exposed to coal slag under conditions typical of those encountered in slagging gasification processes; (B) evaluation of erosion/corrosion-resistant coatings when exposed to prototype operating environments (dropped in FY 78); (C) development, evaluation, and application of nondestructive evaluation methods applicable to coal-conversion systems; (D) evaluation of the corrosion behavior of commercial alloys; (E) development of analytical models to predict the erosive-wear behavior of materials used in coal-conversion plants; and (F) analysis of failed coal-conversion plant components.

Task A -- Evaluation of Ceramic Refractories for Slagging Gasifiers

(C. R. Kennedy, S. W. Kreis, and R. J. Fousek)

To complete the documentation of test run 8 (previously reported in Ref. 1) a chemical analysis of the slag from this test has been performed and is presented in Table I. The slag was acidic in nature with a base-to-acid ratio (B/A) of 0.7 and a ferritic content of 15-18%.

Test run 10, which was funded by a related magnetohydrodynamic program at ANL, has been completed. In this run, a variety of refractories were exposed to a synthetic Montana Rosebud slag with about 10% K_2O content to simulate the effects of the potassium-rich seed. The results of this test are currently being compiled and will be presented in a future quarterly report.

Prior to the initiation of test run 11, which evaluated the corrosion resistance of a variety of refractories to a basic slag, substantial maintenance and repair of the furnace and controls were necessary. This effort included the recasting of the top of the furnace, replacement of several water flow valves, repair of the burner torches, and adjustments to several safety devices. Included in this test were four fused-cast products: alumina (number 2), chrome-spinel (number 22), alumina-chromia (number 280), and magnesia-spinel (number 317). A number of sintered refractories were also tested: three magnesia-chromes (numbers 29, 35, and 41) and four alumina-chromias (numbers 16, 86, 190, and 852). This test was completed in the last week of March 1979; the results will be discussed in the next quarterly report.

To further determine the conditions existing in various coal-gasification pilot plants, samples of slag were obtained from Grand Forks Energy Research Center (GFERC), Grand Forks, ND and from Combustion Engineering (CE), Windsor Locks, CT. The chemical analysis of these samples is shown in Table II. Samples GF-1 and -2 are of a North Dakota Lignite and a Montana Rosebud slag, respectively, from GFERC, whereas samples CE-1 and -2 are of a Pittsbrugh seam coal from two different test runs at CE. The slags from GFERC range from slightly acidic to slightly basic with a ferritic content of ∿ 20%, whereas the slags from CE are more acidic with ferritic contents ranging from 36 to 61%. As previously reported,[1] the ferritic content of slag from the Bi-Gas Pilot Plant in Homer City, PA ranged from 17 to 34%. Therefore, it appears that the effective partial pressure of oxygen in these three pilot plants is in the range of 10^{-2} to 10^{-4} Pa.

TABLE I. Composition of Slag During Corrosion Test Run 8

Component	Exposure Time, h	
	213	518
SiO_2 (S)	37.9[a]	39.0
Al_2O_3 (A)	20.2	20.5
Fe_2O_3 (F_1)	1.4	1.2
FeO (F_2)	4.6	5.2
Fe (F_3)	1.0	0.9
CaO (C)	28.9	28.7
MgO (M)	3.4	2.2
Na_2O (N)	0.8	0.5
K_2O (K)	0.5	0.3
TiO_2 (T)	1.0	1.1
Other	0.3	0.4
B/A Ratio[b]	0.7	0.7
Ferritic Content[c], %	18	15

[a] Wt.%.

[b] Base-to-acid ratio B/A = $(F_1 + F_2 + F_3 + C + M + N + K)/(S + A + T)$.

[c] Ferritic content $= \dfrac{\text{wt.\% } Fe_2O_3}{\text{wt.\% } Fe_2O_3 + 1.11 \text{ wt.\% FeO} + 1.43 \text{ wt.\% Fe}}$.

TABLE II. Compositions of Slag Samples from Pilot Plants

Component	Sample Number			
	CE-1	CE-2	GF-1	GF-2
SiO_2	48.4[a]	46.5	27.5	38.6
CaO	4.7	3.7	32.0	32.9
Na_2O	1.0	1.0	0.4	0.3
K_2O	2.2	1.9	0.5	0.4
MgO	3.0	3.1	4.4	4.3
Fe_2O_3	6.9	12.5	4.2	1.6
FeO	10.6	6.7	16.8	4.3
Fe	0.4	0.5	0.6	0.6
Al_2O_3	21.6	23.0	12.7	15.8
TiO_2	0.9	0.8	0.6	0.9
Other	0.3	0.3	0.3	0.3
B/A Ratio[b]	0.4	0.4	1.4	0.8
Ferritic Content[b], %	36	61	18	22

[a] Wt.%.

[b] As in Table I.

Task C -- Application and Development of Nondestructive Evaluation Methods for Coal-conversion Processes *(W.A. Ellingson, K.J. Reimann, W.J. Shack, and C.A. Youngdahl)*

1. Erosive-wear Detection and Monitoring

a. Metallic Transfer Lines

(1) Ultrasonic Studies - Pilot Plants. The development of ultrasonic instrumentation and techniques for on-line detection of erosion was continued with a second field test of the remote-monitoring system[2] in the automatic-scanning mode under conditions of plant operation at the Bi-Gas pilot plant. Metallographic inspection of sectioned waveguides and attachment welds[3] was performed. An erosion survey of the HYGAS high-pressure cyclone separator[3] was conducted.

The second unattended field test of the automatic erosive-wear detection system was carried out at the Bi-Gas plant beginning October 31. A previous test[2] had demonstrated the capability of the system to retrieve accurate wall-thickness data from carbon steel piping at elevated temperature during plant operation. The test had also revealed some shortcomings of system performance: Data from stainless steel sites at high temperatures had been in poor agreement with expected values, electrical interference had affected the temperature recording at the stainless steel sites, and, because of varying signal amplitudes, an instability in triggering of the pulse-interval timer had occurred. For the second test, a ground loop in the thermocouple circuit was removed and a new thermocouple was installed for the stainless steel sites. Two stainless steel reference blocks equipped with waveguides and transducers were included in the scan sequence and held at room temperature during the test. The strip-chart recorder was placed on a resilient foam pad to reduce any effect of vibration caused by a nearby pump. Stabilization of triggering appears to require an automatic gain control, which was not available; but the instability is transient, and the affected data can be identified and rejected during data reduction. Examples of results obtained from stainless steel waveguide #3, located on a Type 304 stainless steel tee in the product-gas line of the gasifier, are shown in Table III. The system was unattended throughout the eight-day period covered in the table. During this period, no substantial erosion would be expected at the indicated site. An interference-free recording of stainless steel tee temperature was produced. Agreement of thickness results with predicted values was much improved. Addition of automatic gain control to the circuitry to eliminate triggering instability is planned.

A paper, "Ultrasonic Instrumentation Techniques for the Measurement of Erosion of Metallic Components," which concerns the various parameters that affect accurate measurements of wall thickness with the remote scanning system, was written for presentation at the 25th International Instrumentation Symposium, Anaheim, CA, in May 1979. Informational material describing the system has been provided to Techno-Economic Services, Inc., of Los Altos, CA, a consulting firm that is investigating commercial applications. An abstract of a paper describing aspects of long-term erosion measurement by ultrasonic techniques has been submitted to the 12th Symposium on Nondestructive Evaluation, to be held in San Antonio, TX, in April 1979.

Two of the waveguide-attachment weld specimens (described in a previous quarterly report[2]) electric-arc stud-welded by Nelson Division of TRW, Inc. were examined metallographically. The average grain size of a 9.5-mm-diameter stainless steel waveguide was found[4] to be 70 μm, and grain orientations appeared to be random. Welds of this waveguide and of a 15.9-mm-diameter carbon steel waveguide were free of voids and inclusions. Another of the 15.9-mm-diameter guides was therefore reexamined ultrasonically with a 7.5-MHz, 3/8-in.-diameter transducer: a prominent pulse was visible between the reflected pulses from the waveguide shoulder and sample back wall and was identified as a shear-delayed pulse[5] reflected from the shoulder, rather than a weld-produced pulse. Amplitudes of smaller pulses associated with the weld zone were 25% of that of the backwall pulse.

Knurl depth in relation to transducer frequency affects the amplitude of shear-delayed pulses and is being more fully explored. Knurl depth was 0.1 mm for the 15.9-mm-diameter waveguides and 0.2 mm for the 9.5-mm guides of this set. The reduced-diameter portion of all waveguides was 7 mm, and the ratio of this dimension to that of the larger-diameter portion affects the amplitudes of the shoulder and delayed pulses relative to the amplitude of the backwall pulse. The 9.5-mm-diameter guides do not display a prominent delayed pulse with a 7.5-MHz, 3/8-in.-diameter resonant transducer. The knurl depth and diameter ratio of this design are thought to be closer to optimum values.

The HYGAS high-pressure cyclone separator[3] was surveyed at ANL in December 1978 to observe the progress of erosive wear since the previous inspection. Results will be given in the next quarterly report. A paper on the erosion study of the cyclone was written in collaboration with responsible personnel at the HYGAS pilot plant for presentation at the Conference on Erosion/Corrosion of Coal Conversion System Materials held in Berkeley, CA, in January 1979.

TABLE III. Examples of Sh-BW[a] Measurements Obtained by Means of the Erosive-wear Scanning System at a Stainless Steel Fitting in the Gasifier Effluent Line during Pilot Plant Heatup, Operation and Cooldown

Date and Time	Temp.[b] (°C)	k_{ss}[c]	Sh-BW Distance Measured[d] (in.)	Sh-BW Distance Corrected (in.)	Sh-BW Distance Error[e] (mils)
10/31/78					
18:10	50	1.0033	1.365	1.361	-2
20:40	94	1.0095	1.377	1.364	+1
21:50	129	1.0150	1.384	1.364	+1
11/1/78					
06:10	178	1.0222	1.390	1.360	-3
18:15	136	1.0160	1.385	1.364	+1
11/2/78					
02:40	258	1.0345	1.399	1.353	-10
06:15	226	1.0296	1.399	1.359	-4
09:50[f]	365	1.0508	1.413	1.344[g]	-19
12:15[f]	214	1.0277	1.398	1.361	-2
17:10[f]	360	1.0500	1.430	1.362	-1
18:20[f]	369	1.0515	1.427	1.357	-6
11/3/78					
01:30	276	1.0370	1.409	1.358	-5
02:45	179	1.0224	1.384	1.354	-9
06:20	111	1.0123	1.372	1.356	-7
11:15	56	1.0040	1.367	1.362	-1
19:40	40	1.0018	1.364	1.362	-1
11/8/78					
01:30	ambient	1.000	1.357	1.357	-6
05:10	ambient	1.000	1.352	1.352	-11

[a] Distance from reference shoulder of Type 304 stainless steel waveguide to back wall (inner surface) of gasifier-fitting wall, subject to corrections noted.

[b] Temperature of the gasifier fitting, measured by a Type K thermocouple and recorded on the strip chart of the erosive-wear scanner.

[c] Factor to compensate for acoustic-velocity change and thermal expansion of Type 304 stainless steel at elevated temperature, calculated as described in Ref. 2; the distance measured at the stated temperature, divided by this value, yields the value expected at room temperature.

Legend for Table III continues on following page (7).

TABLE III. Examples of Sh-BW[a] Measurements Obtained by Means of the Erosive-wear Scanning System at a Stainless Steel Fitting in the Gasifier Effluent Line during Pilot Plant Heatup, Operation and Cooldown

LEGEND (continued)

[d] Recorded values were converted from chart cm to Sh-BW inches (indicated) by a calibration equation initially determined at room temperature and subsequently adjusted for zero shift with reference to automatic room-temperature measurements of two reference standards that were included in the scan.

[e] Relative to distance of 1.363 in. indicated on a carbon-steel-calibrated scale, without correction for initial $\lambda/2$ offset error. Multiply table values by 0.975 to obtain stainless steel values. An additional error of < 4 mils may be present because of nonoptimized gain setting during unattended scanning. (1000 mils = 1 in. = 25.4 mm).

[f] Plant in operation 08:09-21:28.

[g] Probably includes one $\lambda/2$ shift error relative to the initial value: For the transducer frequency used, the $\lambda/2$ value for stainless steel is 16 mils.

(2) Ultrasonic Studies - Scattering of Acoustic Waves from Rough Surfaces. Rough surface areas of test blocks number 4 through 10 were evaluated by means of ultrasonic scattering. A 5-MHz, 12.7-mm-diameter ultrasonic transducer, operating at a distance of 250 mm (far-field), was used for insonification and detection of reflected echos. Three RF echo-waveforms were recorded from each roughened area. The waveforms were digitized, stored on disc, averaged and their power spectra calculated. From this data, groove depths were calculated by two different methods: (a) temporal separation of echos from groove top and bottom, and (b) interference frequencies in the power spectrum. In Table IV, the calculated results are compared with micrometer measurements.

Some roughened areas in a few blocks were also evaluated for ultrasonic scattering when the beam passes through the thickness of the material. The same experimental conditions were applied to the through-wall scattering as to the scattering from the water/steel interface described above, with the exception of gain setting. The calculated groove depths, derived from through-wall scattering measurements, are given in Table V.

The depth values calculated from ultrasonic scattering correlate quite well with the micrometer measurements. Values obtained from spatial-separation calculations appear to be closer to the measured dimensions than those obtained from interference-frequency calculations. This is mainly caused by the poor resolution of the computer-generated spectral distribution curve. The included angle of the groove has a very strong influence on the spectral distribution as well as the shape of the RF echo signal. The spectrum when viewed on the screen of a spectrum analyzer exhibits complex interference patterns, which suggests that it contains information on groove width. This phenomenon is more pronounced with grooves having rounded-off edges. The temporal resolution of RF echo signals becomes very poor for shallow grooves, making groove-depth estimation impossible. Similarly, large amplitude differences in segments of the RF echo signal yield only very slight modulations of the spectrum, thus inhibiting estimation of groove depth by this method. The limited bandwidth of the transducer can in the case of shallow grooves exhibit only a single interference frequency and groove-depth estimation then becomes guesswork.

Figures 1 and 2 show the ultrasonic waveforms that result when the beam scatters from the water/steel interface and through the material, respectively. It is evident that the latter waveform is more complex. This complexity is caused by wave conversion and multiple passes through the material thickness. During the next quarter, data with transducers of different center frequencies (2.25 and 10 MHz) will be collected. The results should show whether other interference frequencies can be found for shallow grooves. Lower-frequency spectra, using the same number of sampling points, should also result in curves more closely resembling the ones obtained on the spectrum analyzer. A correlation technique will be applied to the ultrasonic RF waveform, which should enable more accurate measurements of time differences in complex waveforms.

TABLE IV. Groove-depth Data from Scattering Measurements at the Water-Steel Interface

Block	Section	Depth (mm)			Error (%)	
		Δt	Δf	Micrometer	Δt	Δf
4	A	0.925	0.925	0.871	6.2	6.2
	B	0.635	unresolved	0.546	16.3	-
	C	unresolved	0.322	0.343	-	5.8
5	A	1.37	1.23	1.43	4.2	14.0
	B	0.814	unresolved	0.83	1.9	-
	C	0.481	unresolved	0.495	2.8	-
6	A	1.80	2.11	1.72	4.7	22.7
	B	1.35	1.23	1.12	20.5	9.8
	C	0.70	0.779	0.724	3.3	7.6
7	A	2.74	unresolved	2.67	2.6	-
	B	unresolved	unresolved	1.60	-	-
	C	0.92	0.925	0.894	2.9	3.5
8	A	2.81	2.96	2.58	8.9	14.7
	B	1.925	1.99	1.72	11.9	15.8
	C	1.035	1.076	1.02	1.5	5.5
9	A	unresolved	3.17	3.99	-	20.6
	B	unresolved	1.85	2.47	-	25.1
	C	1.41	1.30	1.36	3.7	4.4
10	A	4.66	4.44	4.7	0.9	5.5
	B	3.15	3.08	3.17	0.6	2.8
	C	1.55	1.55	1.58	1.9	1.9

TABLE V. Groove-depth Data from Scattering Measurements Though the Material Thickness

Block	Section	Depth (mm)			Error (%)	
		Δt	Δf	Micrometer	Δt	Δf
4	A	0.855	0.693	0.871	1.8	20.4
5	B	0.70	0.713	0.83	15.7	14.1
8	A	2.43	3.56	2.58	5.8	38.0
	B	1.57	1.63	1.72	8.7	5.2
	C	1.0	0.847	1.02	2.0	17.0
9	D	2.43	3.00	2.47	1.6	21.5
10	B	3.00	3.17	3.17	5.4	0

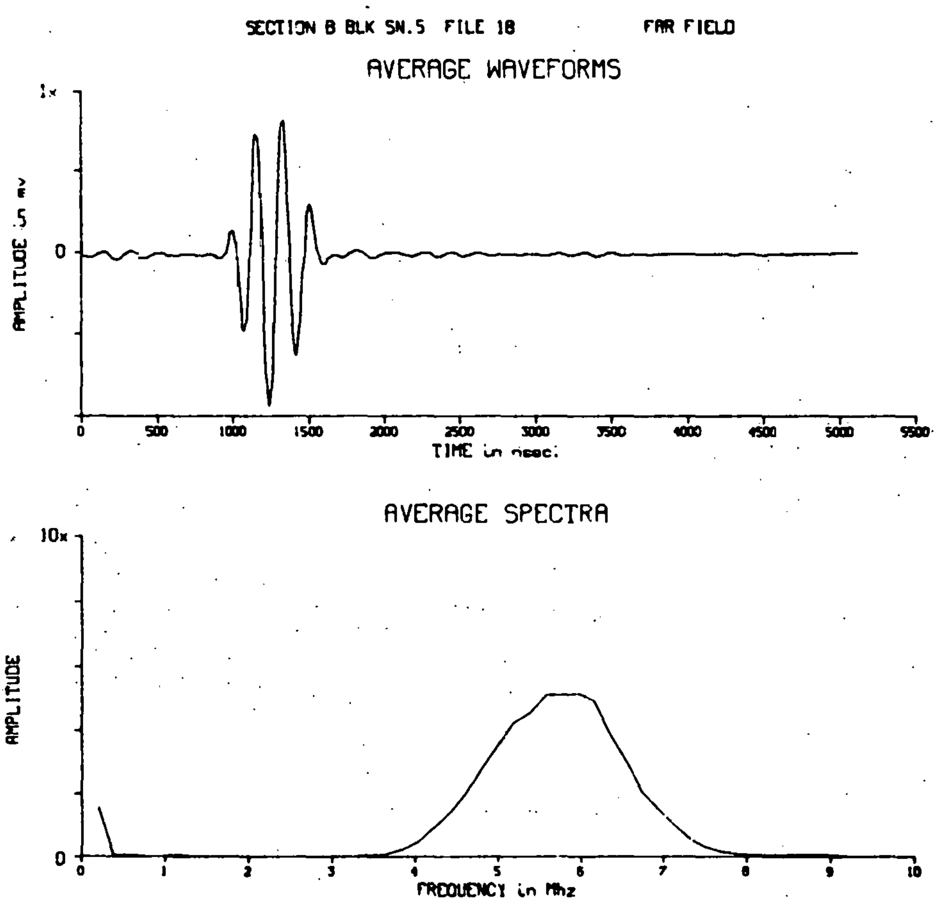

Fig. 1. Scattering from Rough Surface at Water-Steel Interface. ANL Neg. No. 306-79-174.

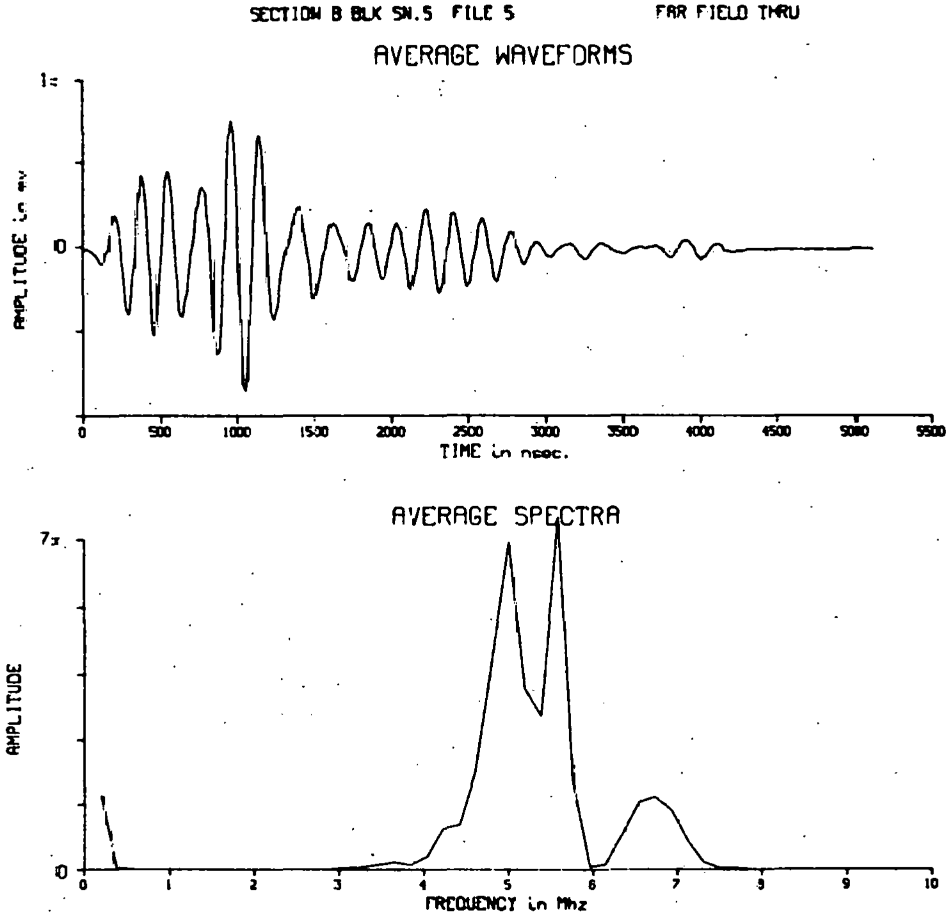

Fig. 2. Scattering from Same Rough Surface Shown in Fig. 1, with Beam Going Through the Material (Steel). ANL Neg. No. 306-79-173.

2. Refractory Installation Practices

a. Detection of Thermally Induced Acoustics from Refractory Concrete Materials

The panel fired last quarter has been examined and data analysis is continuing. New refractory materials using fibre reinforcing (small wires) are being considered for tests using acoustic emission. The computer program for real-time calculation of characteristic slope was also modified this quarter.

3. Component Inspection

a. Acoustic Monitoring of Valves

Two acoustic instruments for valve-leak testing[2,3], which had been installed by ANL in the valve-leak test facility at the Morgantown Energy Technology Center (METC), were operated by ANL during an METC valve-test sequence (#A-19)* on October 17-18, 1978. The purpose of the ANL activity was to field test the response of the acoustic instruments to known amounts of nitrogen gas leakage in a large, high-pressure valve.

The valve being tested by METC was a new 6-in., 4.1 MPa- and 316-rated, EPG ball valve made for coal slurry service. The valve body was of carbon steel, the ball and stem of stainless steel/tungsten carbide, and the seat of stellite.

A part of the initial room-temperature valve-testing sequence consisted of pressurizing the inlet side with the valve closed and the outlet-side pressure at one atm, checking for inlet-side pressure loss, cycling the valve open and closed, and repressurizing the inlet side to begin a repetition of the cycle.

When the pressure-loss measuring steps were done under operator control, rather than by the automatic-cycling controller, opportunities existed to obtain sensitive readings of acoustic noise caused by gas flowing from small leaks within the valve. At such times extraneous signals caused by gas flow in other parts of the test system were virtually absent except for a steady background signal that could be detected with the system pressurized and the valve unpressurized. It was assumed that, when the test-valve inlet was pressurized and the pressurizing valve was again closed, the background signal value was unchanged. Increases in signal level above the background level were attributed to leakage across at least one of the body-to-ball seals of the test valve, because valve-packing leakage was eliminated prior to the test and was found to be insignificant in subsequent checks.

Our instrumentation consisted of an acoustic valve-leak detector (AVLD) provided by the Naval Ship Research and Development Laboratory and a prototype acoustic-signal analyzer, model AET 204B, supplied by Acoustic

---

*METC Project Engineer: J.F. Gardner

Emission Technology Corporation (AETC). Both instruments were described previously.[3] Two acoustic transducers were coupled to the connecting flange on the outlet side of the test valve: for each pickup a brass disk was epoxied with one face in acoustic contact with the flange, electrical isolation of the disks from the flange was verified, and one transducer was coupled face-to-face to each disk with silicone vacuum grease. Each transducer was held in place with a spring-loaded clamp engaged in a groove that had been provided at the edge of each disk. For the AVLD the transducer was an Endevco 2217E accelerometer, and for the AETC unit, an AETC 175-KHz resonant acoustic-emission transducer. The AVLD amplifier and the AETC preamplifier were located near the transducers and were connected to a readout station external to the test cell. The AVLD frequency dial was set to 51 KHz, and the attenuator was set to provide a 120-dB gain; the bandwidth was ± 5 KHz. The AETC unit was set to provide a bandwidth from 90 to 330 KHz, with a system gain of 108 dB. The rms outputs of the two units were read on Simpson meters.

Results of valve leakage tests made after 123 previous test cycles are shown in Table VI. A background value of 0.7 V has been subtracted from each AVLD reading to obtain the table values. For AETC data, 0.81 V background was subtracted and the results were adjusted to a 120-dB gain. The associated gas-flow values were obtained from pressure and pressure-change-rate data measured by METC[6], with known volumes of valve and system.

As the table shows, usable indications of small leaks occurred with both acoustic units and increased with greater leak rate. The two units would be expected to differ with respect to immunity to low-frequency, structure-borne noise; but in-plant testing is needed to explore this distinction quantitatively. In the tests both units were subject to interference by occasional airborne noise, and means of reducing such interference are being considered. However, a lower gain setting would probably be used to monitor for leakages near the value of in-plant operational interest which has been defined as 60 scfm, at 1000 psi ΔP (0.028 m^3/s S.T.P. at 6.9 MPa) for a 6-in. valve. Means of localizing the source of leakage are being studied.

A paper describing the laboratory and field studies under this program related to nonintrusive measurements of gas-valve leakage by passive acoustic techniques has been written for presentation at the 25th International Instrumentation Symposium, Anaheim, CA, May 1979.

TABLE VI. Acoustic Response to Gas Leakage in a 6-in., 4.1 MPa- and 316°C-rated Ball Valve for Two Acoustic Instruments[a]

Valve Pressure[b]		Leak Rate		rms Acoustic Response[c], V	
MPa (gage)	psig	10^{-6} m^3/s (S.T.P.)	scfm	AETC	AVLD
0.34	50	0.3	0.00073	0	0
2.79	404	6.1	0.013	0.04	0.2
3.45	500	23.5	0.0497	0.16	0.7
4.05	588	99.9	0.2116	0.56	1.5

[a] Room-temperature tests

[b] On high-pressure side (low-pressure side held at 1 atm).

[c] After subtraction of background response and adjustment to 120-dB gain. Instrument settings are given in text.

Task D -- Corrosion Behavior of Materials

1. Corrosion in Gasification Environments *(K. Natesan)*

The objectives of this program are to (1) develop uniaxial tensile data on four commercial alloys upon exposure to multicomponent gas environments, (2) experimentally evaluate the high-temperature corrosion behavior of iron- and nickel-base alloys in gas environments with a wide range of oxygen, sulfur, and carbon potentials, and (3) develop a systems approach, based upon available thermodynamic and kinetic information, to evaluate possible corrosion problems in different coal-conversion processes.

The experimental program to generate uniaxial tensile data on four iron- and nickel-base alloys upon exposure to multicomponent gas environments was discussed previously.[7] The experimental apparatus and the chemical composition of the alloys and gas mixtures used in this program were described in detail.[1] Calculated values for the oxygen and sulfur partial pressures established by the gas mixtures in different runs have also been reported.[3]

During the present quarter, uniaxial tensile specimens, which were thermally aged for 3.6 Ms (1000 h) at 750, 871, and 982°C, were tensile tested in vacuum at an initial strain rate of $4.1 \times 10^{-4}\ s^{-1}$. Additional experiments that involve the exposure of corrosion and uniaxial-tensile specimens to gas mixture 2B (see Ref. 1) for 3.6 Ms (1000 h) at 750 and 871°C were completed. Also, 3.6-Ms exposures of specimens to gas mixtures 3A and 3B at 982 and 750°C are in progress.

Tensile data for the thermally aged specimens can be compared with earlier results[3] from specimens exposed to mixed-gas environments to determine the changes in the tensile properties due to variations in oxygen and sulfur partial pressures in the gas environment. Figures 3-6 show the engineering stress-engineering strain curves for Incoloy 800, Type 310 stainless steel, Inconel 671, and U.S. Steel Alloy 18-18-2, respectively, in the as-received and thermally aged conditions, and after 3.6-Ms exposure to gas mixtures with different oxygen, sulfur, and carbon potentials at 750°C. In general, the results show that the ultimate tensile strength decreases after exposure to complex gas mixtures when compared with those of the material (except Inconel 671 alloy) in the as-received and thermally aged conditions. In the case of Inconel 671, which is a two-phase nickel-base alloy containing 48 wt.% Cr and 0.35 wt. % Ti, thermal aging of the material at 750°C has a strong effect on the tensile behavior, as shown in Fig. 5. Exposure of this alloy to the complex gas mixtures primarily increases the tensile ductility values, as can be seen from Fig. 5. The load-elongation data from the tensile tests were also converted to true stress-true strain curves up to the point of maximum engineering stress by assuming a constant-volume approximation for the tensile deformation. Figures 7-10 show the true stress-true strain curves for Incoloy 800, Type 310 stainless steel, Inconel 671, and U.S. Steel Alloy 18-18-2, respectively, in the as-received and thermally aged conditions, and after 3.6-Ms exposure to gas mixtures with different oxygen, sulfur, and carbon potentials at 750°C. In general, the flow stress of the material decreases after exposure to complex gas mixtures when compared with those of the material in the as-received and thermally aged conditions. The decrease in flow stress with a decrease in oxygen partial pressure is much more pronounced for the Fe-Cr-Ni alloys (Incoloy 800, Type 310 stainless steel, and U.S. Steel Alloy 18-18-2) than for the nickel-based alloy (Inconel 671).

a. Effect of Gas Chemistry on Corrosion

The experimental program on the corrosion of materials in multicomponent gas environments has clearly established the requirement that viable alloys must develop protective oxide scales on exposure to complex gas mixtures since the growth rates of sulfide or carbide layers are orders of magnitude larger than that of oxide layers and lead to unacceptable corrosion rates. In view of this, iron-, nickel-, and cobalt-base alloys with stable oxide formers such as chromium and aluminum as major constituents are of interest for application in elevated-temperature regions of a gasifier. To develop protective oxide scales on a given alloy, it is essential to establish the influence of oxygen partial pressure in the gas environment on the morphology of corrosion-product layers. The interrelationship among oxygen and sulfur partial pressures in the gas phase, alloy chemistry, and test temperature and pressure is of considerable interest in establishing the critical oxygen pressures (if any) that are required to achieve a stable, adherent oxide scale on the metal surface. For this purpose, experiments are being conducted on a number of Fe-Cr-Ni alloys with a wide range of Cr and Ni contents in mixed-gas environments. In general, the oxygen and sulfur partial pressures are varied over a wide range of interest in coal-conversion systems. The specimens are subsequently examined to evaluate the type and morphology of the corrosion-product layers and thicknesses of the scale layer and internally affected region.

Figure 11 shows the experimental results obtained for Type 310 stainless steel in complex gas mixtures at 982 and 1000°C. The figure, which includes the results of a number of investigators,[8-11] clearly shows that for a given sulfur partial pressure, there exists a threshold oxygen partial pressure beyond which a continuous protective oxide scale is developed on the specimens. This threshold oxygen partial pressure, represented by the kinetic boundary in the figure, is $\sim 10^3$ times the oxygen partial pressure for the Cr oxide/Cr sulfide equilibrium. Similar experimental results for Incoloy 800 obtained at 982 and 1000°C from the work of different investigators[8-10,12] are shown in Fig. 12. Most of the data points in Figs. 11 and 12 are based on 0.09 to 0.18-Ms (25 to 50-h) exposures in complex gas mixtures; however, some data from this study and the work of Hill et al. are from longer-time experiments, e.g., 3.6 Ms (1000 h). The threshold oxygen partial pressure values are much larger for these long-term data, which seems to indicate that the corrosion behavior of material is influenced by the extent of sulfur diffusion through the oxide scale and the formation of sulfides underneath the scale, which subsequently affects the adherence of the scale to the base metal. This probably explains the breakaway corrosion that has been observed in a number of alloys exposed to complex gas atmospheres. For example, Hill et al. observed corrosion rates of ~ 75 μm and 2.0 mm after 3.6 Ms (1000 h) and 7.2 Ms (2000 h), respectively, even though the oxygen, sulfur, and carbon potentials and temperature were maintained the same. Such catastrophic breakaway corrosion rates have been analyzed by

Natesan and Delaplane[12] for Incoloy 800. They examined the corrosion behavior of Incoloy 800 relative to the ratio $p_{O_2}/p^e_{O_2}$, where p_{O_2} and $p^e_{O_2}$ are the oxygen partial pressures in the gas mixture and for the Cr oxide/Cr sulfide equilibrium, respectively. Figure 13 shows the effect of variation in $(p_{O_2}/p^e_{O_2})$ ratio on the scale thickness and alloy penetration depth for Incoloy 800 after 0.09-Ms exposure at temperatures between 750 and 1000°C to gas mixtures with a wide variation in oxygen and sulfur partial pressures. It is interesting to note that irrespective of temperature and sulfur partial pressure in the range of our investigation, there exists a threshold oxygen partial pressure $p_{O_2}/p^e_{O_2} \simeq 10^3$ above which the scale thickness and alloy penetration depths are negligibly small. The effect of exposure time on the breakaway corrosion has also been analyzed.[12] The results for Incoloy 800, shown in Fig. 14, indicate that as the exposure time increases, a greater threshold oxygen partial pressure is required to prevent breakaway corrosion.

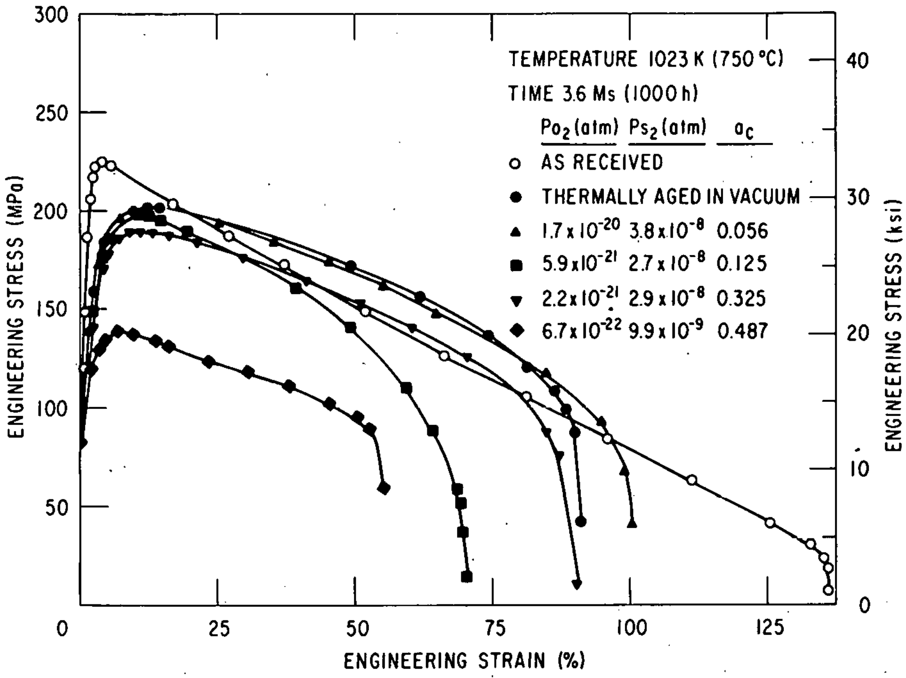

Fig. 3. Engineering Stress-Engineering Strain Behavior for Incoloy 800 in the As-received and Thermally Aged Conditions and After 3.6-Ms Exposures to Complex Gas Mixtures at 750°C. ANL Neg. No. 306-79-96.

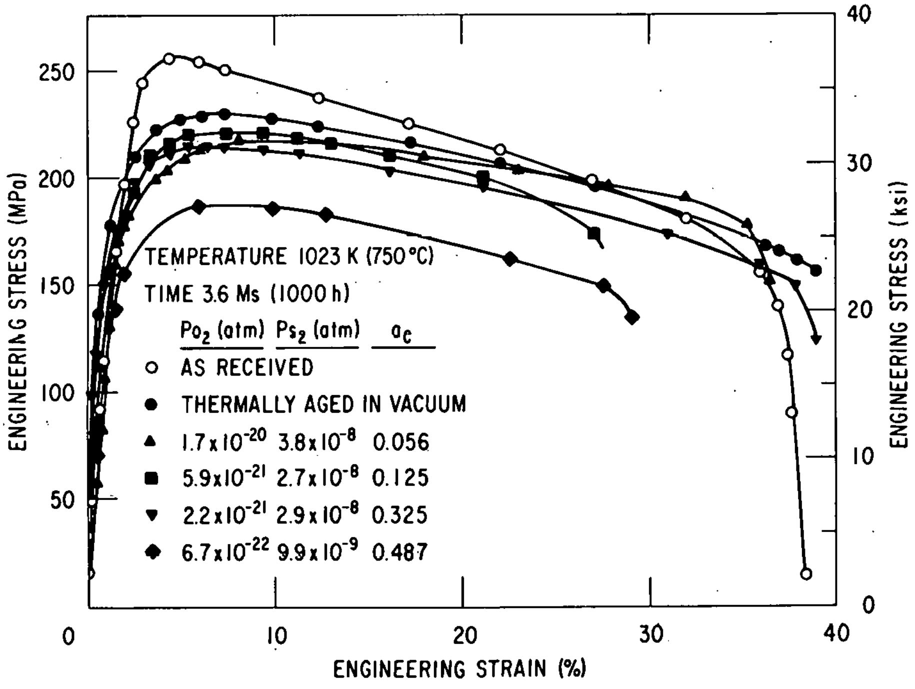

Fig. 4. Engineering Stress-Engineering Strain Behavior for Type 310 Stainless Steel in the As-received and Thermally Aged Conditions and After 3.6-Ms Exposures to Complex Gas Mixtures at 750°C. ANL Neg. No. 306-79-78.

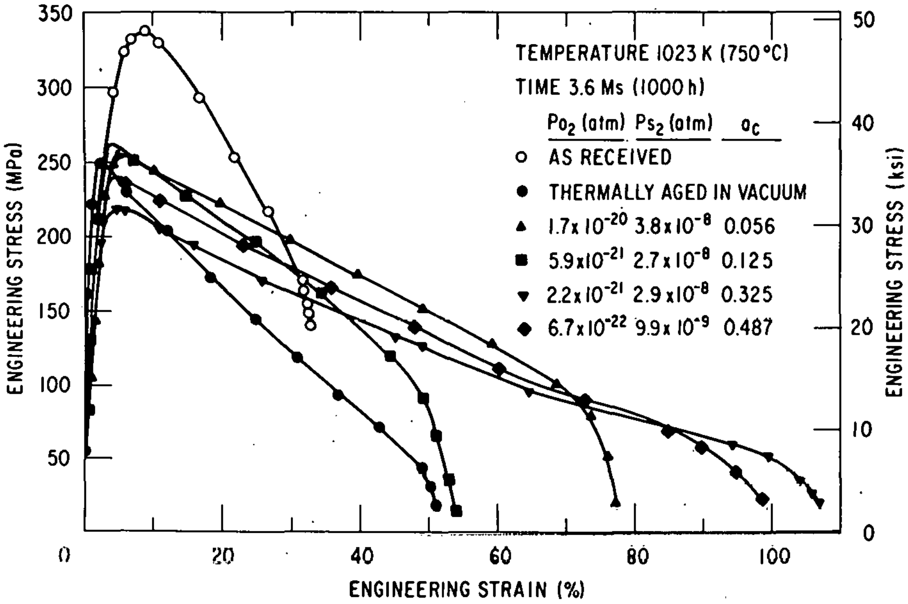

Fig. 5. Engineering Stress-Engineering Strain Behavior for Inconel 671 in the As-received and Thermally Aged Conditions and After 3.6-Ms Exposures to Complex Gas Mixtures at 750°C. ANL Neg. No. 306-79-94.

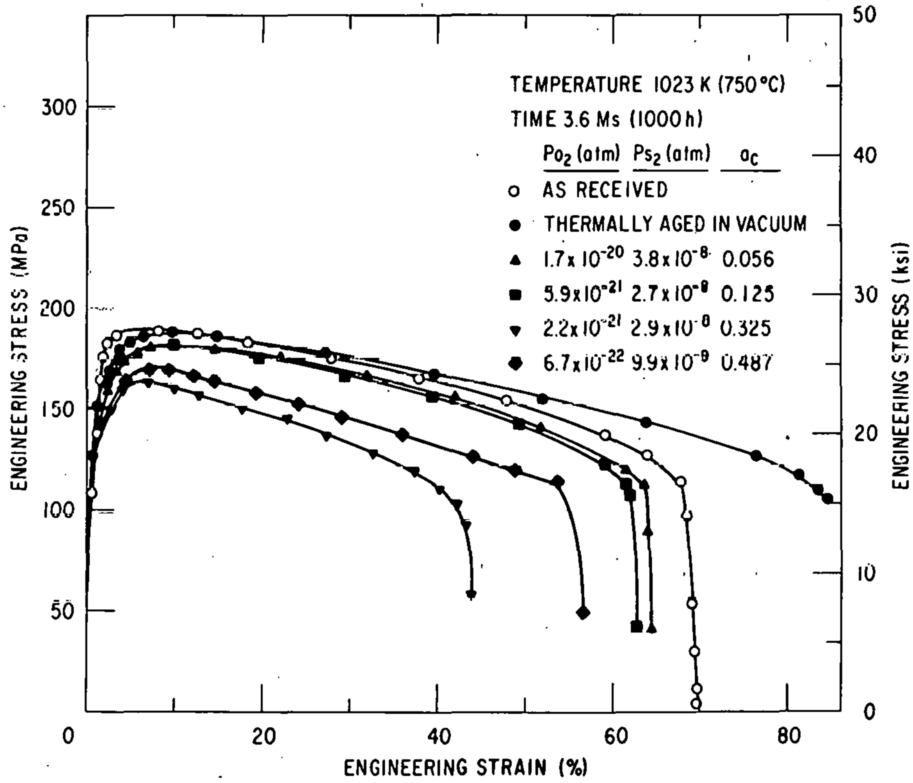

Fig. 6. Engineering Stress-Engineering Strain Behavior for U.S. Steel Alloy 18-18-2 in the As-received and Thermally Aged Conditions and After 3.6-Ms Exposures to Complex Gas Mixtures at 750°C. ANL Neg. No. 306-79-79.

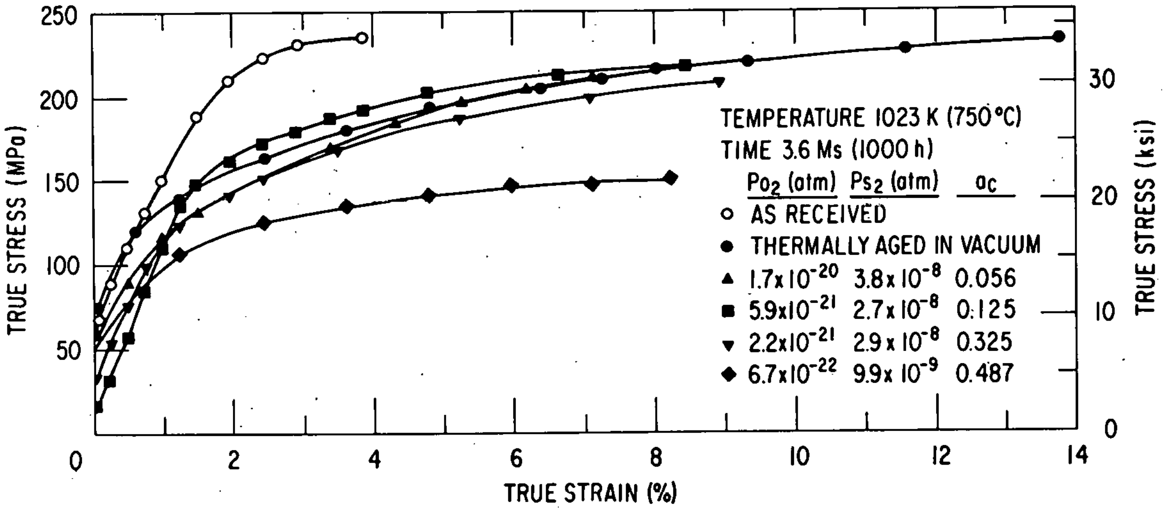

Fig. 7. True Stress-True Strain Behavior (up to the Point of Maximum Engineering Stress) for Incoloy 800 in the As-received and Thermally Aged Conditions and After 3.6-Ms Exposures to Complex Gas Mixtures at 750°C. ANL Neg. No. 306-79-83.

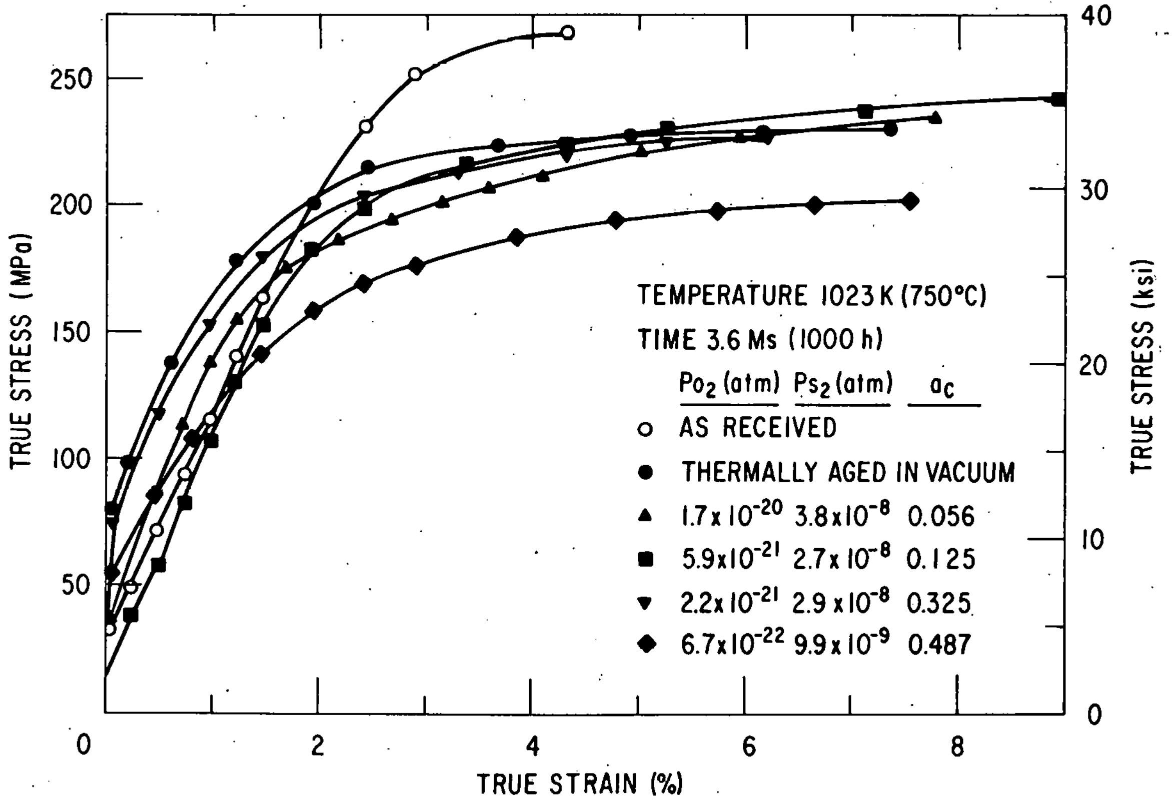

Fig. 8. True Stress-True Strain Behavior (up to the Point of Maximum Engineering Stress) for Type 310 Stainless Steel in the As-received and Thermally Aged Conditions and After 3.6-Ms Exposures to Complex Gas Mixtures at 750°C. ANL Neg. No. 306-79-97.

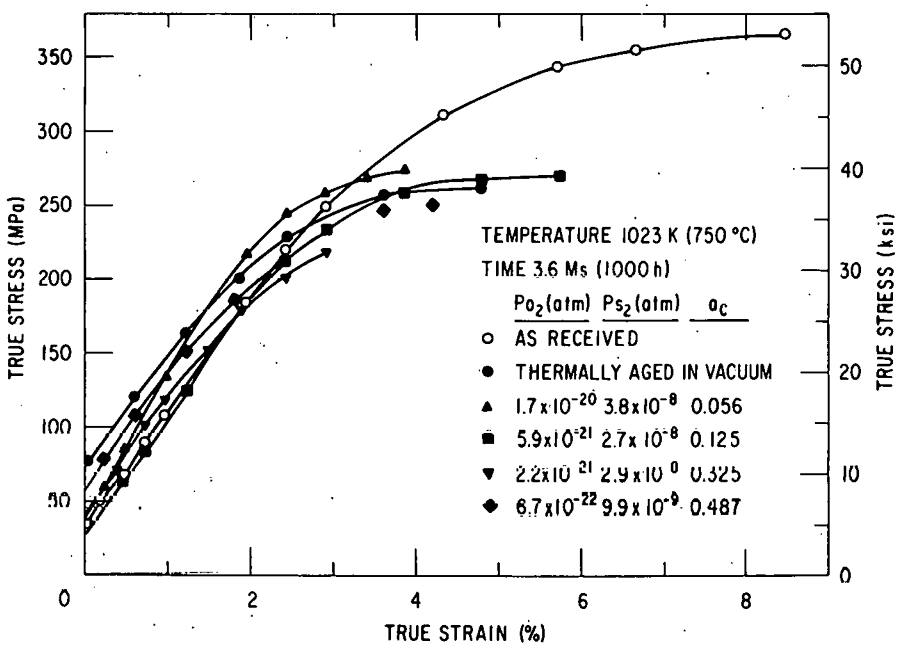

Fig. 9. True Stress-True Strain Behavior (up to the Point of Maximum Engineering Stress) for Inconel 671 in the As-received and Thermally Aged Conditions and After 3.6-Ms Exposures to Complex Gas Mixtures at 750°C. ANL Neg. No. 306-79-87.

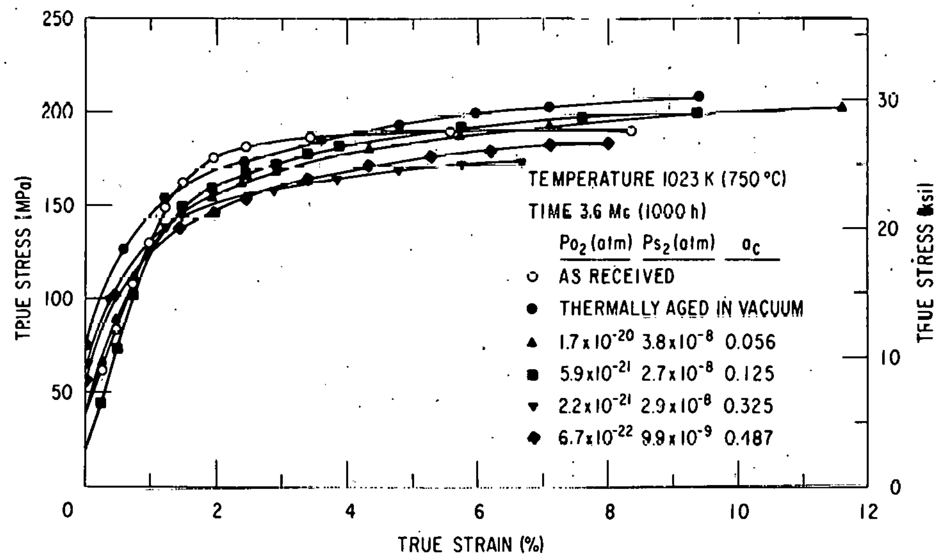

Fig. 10. True Stress-True Strain Behavior (up to the Point of Maximum Engineering Stress) for U.S. Steel Alloy 18-18-2 in the As-received and Thermally Aged Conditions and After 3.6-Ms Exposures to Complex Gas Mixtures at 750°C. ANL Neg. No. 306-79-92.

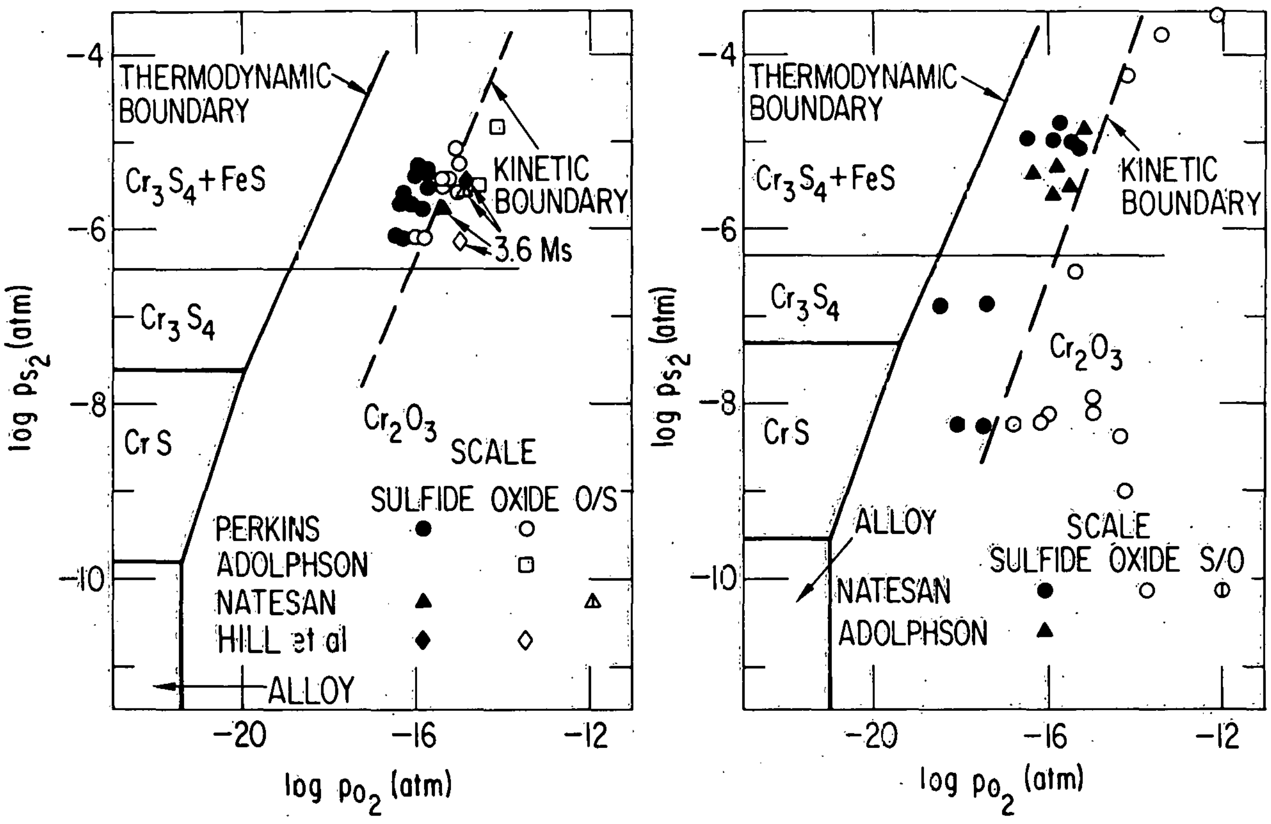

1255 K (982 C)

1273 K (1000 C)

Type 310 Stainless Steel

Fig. 11. Experimental Data on the Types of Scale Developed on Type 310 Stainless Steel as a Function of Oxygen and Sulfur Partial Pressures in the Gas Environment. ANL Neg. No. 306-79-36 R.

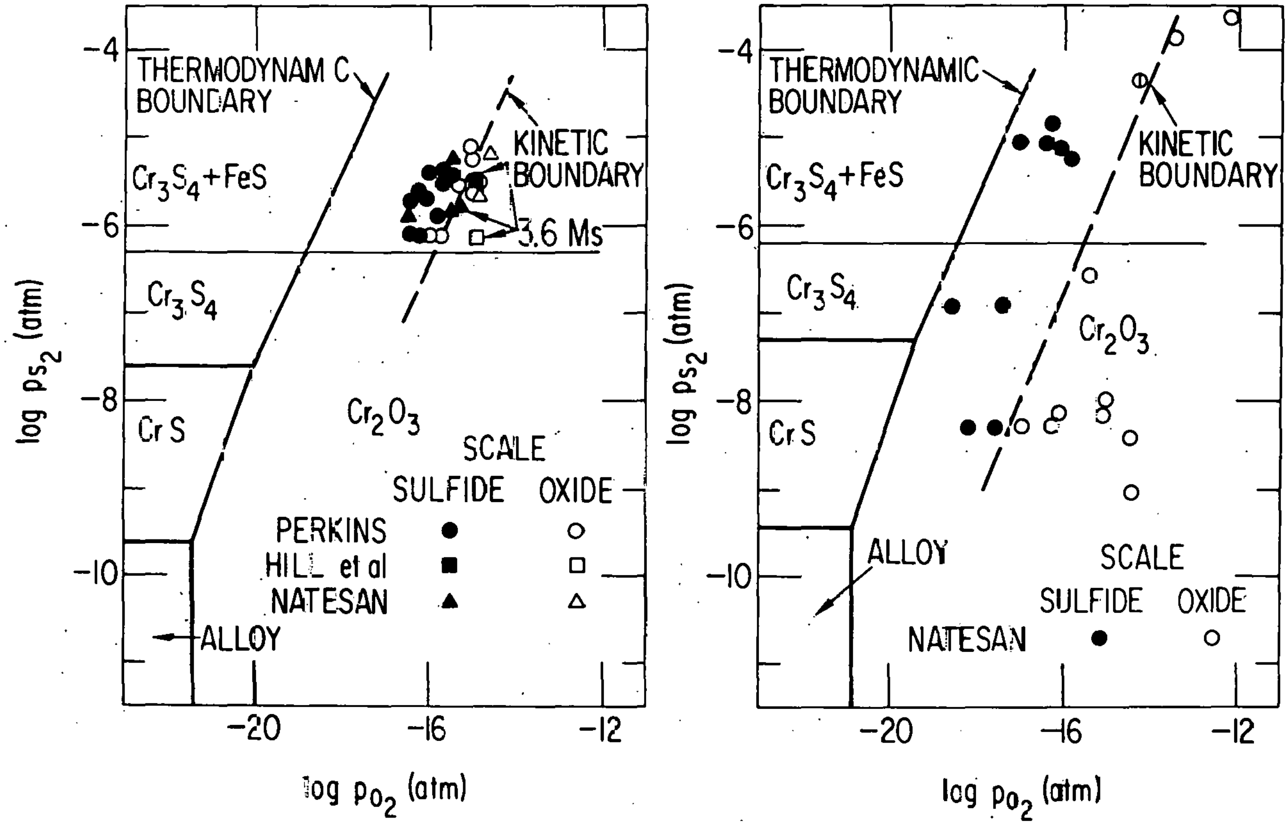

1255 K (982 C) 1273 K (1000 C)

Incoloy 800

Fig. 12. Experimental Data on the Types of Scale Developed on Incoloy 800 as a Function of Oxygen and Sulfur Partial Pressures in the Gas Environment. ANL Neg. No. 306-79-35 R.

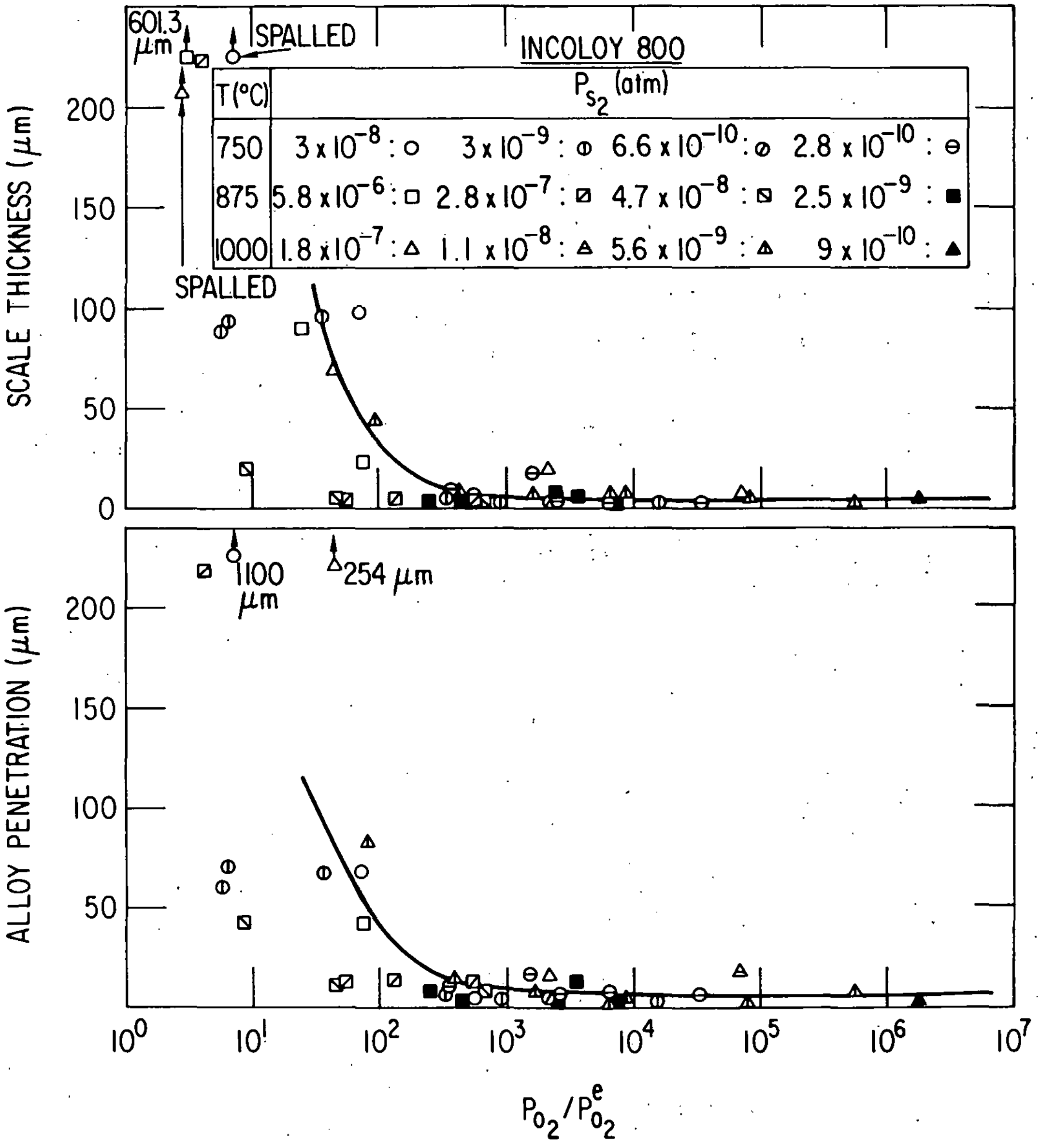

Fig. 13. Variation in Scale Thickness and Alloy Penetration Depth as a Function of an Excess Parameter $p_{O_2}/p^e_{O_2}$ for Incoloy 800 Exposed to Complex Gas Environments. p_{O_2} and $p^e_{O_2}$ are the oxygen partial pressures in the experimental gas mixture and at the Cr sulfide/Cr oxide phase boundary, respectively. ANL Neg. No. 306-78-918 R.

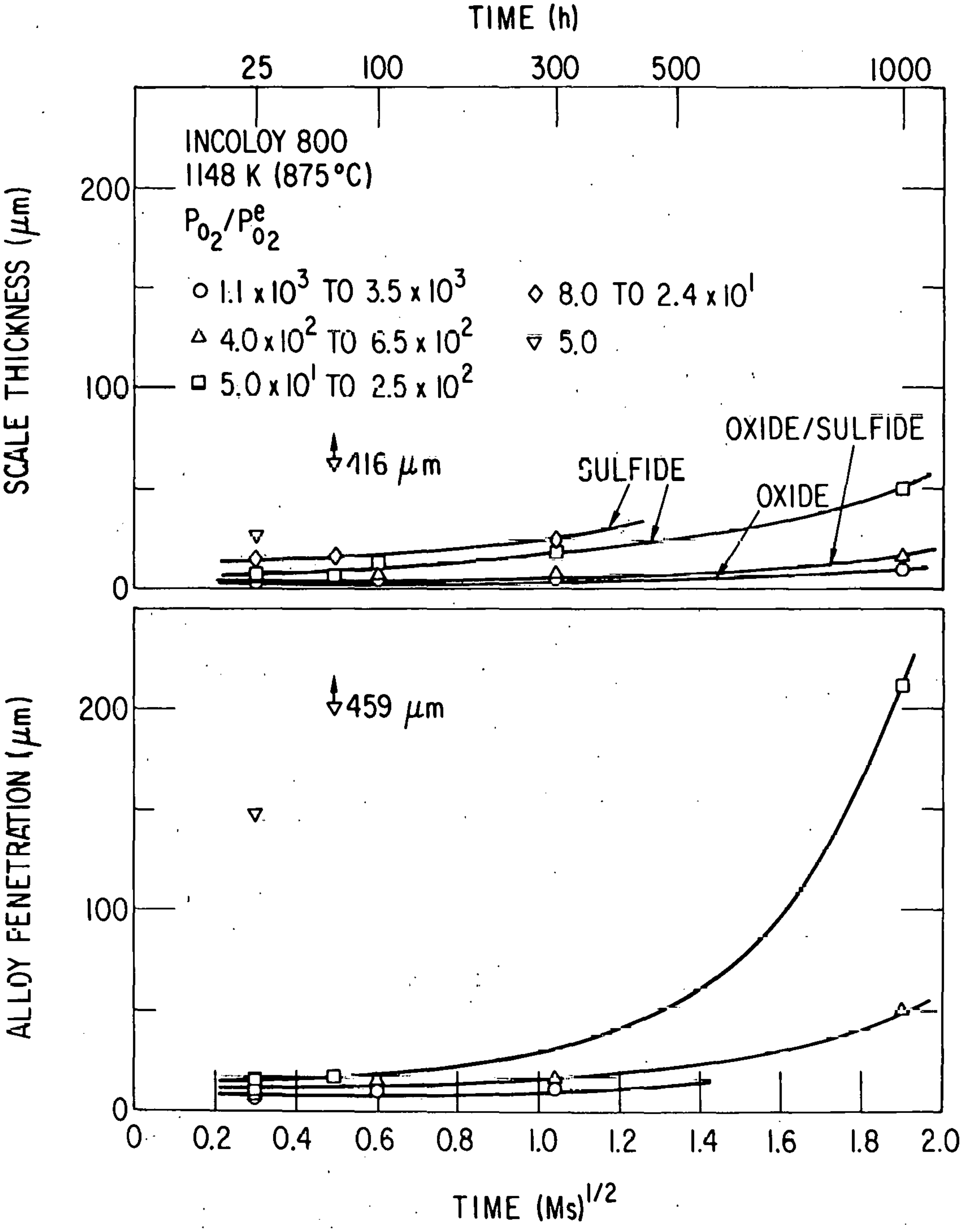

Fig. 14. Effect of Exposure Time on the Scale Thickness and Alloy Penetration Depth for Incoloy 800 as a Function of the Oxygen Partial Pressure Ratio $p_{O_2}/p^e_{O_2}$. ANL Neg. No. 306-78-919 R.

2. Effect of Sulfation Accelerators and Corrosion Inhibitors on Materials in Fluidized-bed Combustion Systems *(O.K. Chopra)*

a. Introduction

The sulfation rate and the extent of sulfation of many limestones can be enhanced by impregnating the stone with salts (i.e., sulfation accelerators) such as NaCl, $CaCl_2$, or Na_2CO_3. The presence of salt induces structural rearrangements in the stone, which lead to an optimum pore distribution for reaction with SO_2-O_2 mixtures.[13] The major effect of salt addition involves the formation of a liquid film on the surface of the CaO grains, which increases the ionic mobility of the reactants. Enhanced diffusion facilitates rearrangement and recrystallization of CaO and $CaSO_4$ grains and consequently allows more sulfation to occur.

A high capacity for sulfur retention would decrease the quantity of limestone required for the combustion process and would lower the process cost as well as reduce the environmental impact of solid waste disposal. However, the use of sulfation accelerators in fluidized-bed combustion systems requires an evaluation of the possible effects of these constituents on the corrosion of structural materials to identify factors that could decrease the reliability and lifetime of system components.

The objectives of this program are to (a) evaluate the effect of sulfation accelerators on the corrosion behavior of candidate materials for an atmospheric-pressure fluidized-bed combustion system, (b) measure the oxygen activity in the fluidized bed and freeboard, (c) determine the types of deposits formed on metal surfaces, (d) study the nature of the corrosion reactions resulting from these deposits, and (e) correlate the corrosion results with the process conditions to define maximum limits for constituents that are responsible for accelerated corrosion of plant materials.

b. Fluidized-bed Combustion Facility and Corrosion Tests

The process development unit (PDU), atmospheric-pressure fluidized-bed coal-combustion facility (AFBC) at Argonne National Laboratory was used for conducting the corrosion tests. A schematic diagram of the AFBC facility is shown in Fig. 15. Major components of the facility consist of air preheater, a 152-mm-diameter atmospheric-pressure cumbustor, coal and limestone-sorbent hopper-feeder assemblies, two parallel off-gas particulate removal systems, and an off-gas analysis system. A detailed description of the major components of the facility is given elsewhere.[14] The nominal operating conditions for combustion are listed in Table VII.

The composition of the materials used for the corrosion studies is given in Table VIII. Two types of corrosion specimens were fabricated from the various materials. Tubular ring specimens, 22.2 mm in diameter and 22.2 mm long, were used with the air-cooled corrosion probes and ∿ 8-mm-thick disk specimens were used with uncooled corrosion-coupon holders. Schematic diagrams of the air-cooled probe and coupon holder are shown in Figs. 16 and 17, respectively. For each corrosion test, three air-cooled probes and four coupon holders, each holding seven corrosion specimens, were installed at various locations in the fluidized-bed and freeboard sections of the combustor. The temperature along the length of the air-cooled probes was recorded at three locations, i.e., at the two end specimens and the center specimen. The temperature differential between the cooling air inlet and outlet for the air-cooled probes was approximately 100°C.

Three 360-ks (100-h) corrosion tests have been completed in the atmospheric-pressure fluidized-bed combustor. The experimental conditions for these tests are given in Table IX. In tests CT-2 and CT-3, NaCl or $CaCl_2$ salt was introduced in the fluidized bed by treating the limestone in salt solution and drying. The materials, specimen location, and temperature of the corrosion specimens for the three runs are given in Tables X-XII.

c. Results

The top and bottom view of the air-cooled probes and coupon holders from the three corrosion tests are shown in Figs. 18-23. The surfaces of the corrosion coupons are shown in Figs. 24-26. The air-cooled tubular specimens and the flat coupons, which were placed inside the fluidized bed, had thin oxide scales and 20- to 30-mm-thick surface deposits from the bed material. Some of the surface scale spalled during cooling. The corrosion specimens that were placed in the freeboard section of the combustor had a fine powdery deposit on the bottom surfaces and a loose particulate deposit on the top surfaces. The deposits from the various corrosion specimens are being identified by x-ray diffraction and electron microprobe analysis.

The corrosion specimens are being examined metallographically to evaluate the extent of corrosion as a function of temperature and location in the combustor. Metallographic examination of the corrosion coupons placed inside the fluidized bed has been completed for the three test runs. The corrosion behavior of these specimens was evaluated by measuring the average thickness of the surface scale and the average depth of internal corrosive penetration at the side surfaces and the top and bottom edges of the specimens. Values for the thickness of the surface scale and internal corrosive penetration for specimens from the three corrosion tests are given in Tables XII-XV. The average temperature of the specimens in these tests was ∿ 845°C.

All the corrosion specimens that were examined had a 2- to 3-μm-thick oxide scale on the surface. The internal corrosive penetration consisted primarily of internal oxidation along the grain boundaries and carbide particles and patches of sulfides ahead of the oxidation front. Internal corrosion along the top and bottom edges of the nickel-base alloys was generally greater than that along the side surfaces. This difference in the corrosion behavior is due to the position of the corrosion coupons in the fluidized bed, viz., the side surfaces are parallel and the top/bottom edges are perpendicular to the flow of the fluidizing gas and bed material.

The average thickness of surface scale and internal corrosive penetration measured on the side surfaces of the specimens are shown in Figs. 27 and 28 for specimens located 102 and 610 mm above the fluidizing-gas distributor plate, respectively. In the absence of salt, the total corrosion, i.e., the combined value of the thickness of surface scale and internal corrosive penetration, for the various materials varies from 7 to 15 μm. It should be noted that although the values of total corrosion for Inconel 601, Inconel 617, and Inconel 671 specimens shown in Figs. 27 and 28 are small, the internal corrosive attack in some areas of these specimens was significantly greater. The results for the corrosion tests in which salt was present show that for all materials, the addition of 0.3 mol % $CaCl_2$ to the fluidized bed has no effect on the corrosion behavior. In fact, for most of the materials, the total corrosion is slightly lower than that without salt addition. However, addition of 0.5 mol % NaCl increases the total corrosion in all the materials. The high-nickel alloys, viz., Inconel 601, Inconel 617, Inconel 671, RA 333, and Incoloy 800 show significant increase in internal corrosive penetration.

Examination of the data for Type 310 stainless steel from the three corrosion tests shows that the total corrosion of this material is greater at the location 102 mm above the gas distributor plate (Fig. 27) than at the 610-mm position (Fig. 28). Similar comparisons for other materials will provide a better understanding of the effect of position within the combustor on the corrosion behavior.

d. Conclusions

Results from the 360-ks tests indicate that the addition of 0.3 mol % $CaCl_2$ to the fluidized bed has no effect on the corrosion behavior of the various materials. The addition of 0.5 mol % NaCl increases the corrosion rates of all the materials. In the presence of NaCl, austenitic stainless steels and Haynes alloy 188 exhibit better corrosion resistance than the high-nickel alloys, although Hastelloy-X, Inconel 625, and Inconel 718 also show good resistance to accelerated corrosion. Longer-duration tests are being considered to further evaluate the effect of salts on the corrosion behavior of various structural materials.

TABLE VII. Nominal Operating Conditions for Atmospheric Fluidized-bed Combustor

Process Variable	Nominal Value
Fluidized-bed Temperature	855°C (1571°F)
Pressure	152 kPa (1.5 atm)
Superficial Fluidizing Velocity	1 m/s (3.3 ft/s)
Coal Feed Rate[a]	895 mg/s (7.1 lb/h)
Limestone Feed Rate[b]	428 mg/s (3.4 lb/h)
Heat Generation Rate	26.3 kJ/s (89,800 BTU/h)
Fluidized Bed Height	813 mm (32 in.)
Fluidizing-combustion Air Flow Rate	6.8 mm^3/s (14.4 scfm)
Estimated Coolant Air Required	18.9 mm^3/s (40 scfm)

[a] Based on Eastern bituminous coal, such as Sewickley.

[b] Based on Greer limestone. Ca/S mole ratio = 3.

TABLE VIII. Composition[a] of Candidate Materials

	Fe	Ni	Cr	Co	Mo	Mn	Si	C	Others
Cobalt Base									
Haynes 188	1.6	22.9	21.5	Bal.	-	0.9	0.4	0.10	13.6 W, 0.06 La
Nickel Base									
Inconel 601	14.1	Bal.	23.0	-	-	0.5	0.25	0.05	1.35 Al, 0.25 Cu
Inconel 617	-	Bal.	22.0	12.5	9.0	-	-	0.07	1.0 Al
Inconel 625	2.5	Bal.	21.5	-	9.0	0.25	0.25	0.05	3.6 Nb, 0.2 Al, 0.2 Ti
Inconel 671	-	Bal.	48.0	-	-	-	-	0.05	0.35 Ti
Inconel 718	18.5	Bal.	19.0	-	3.0	0.18	0.18	0.04	5.1 Nb, 0.9 Ti, 0.5 Al, 0.2 Cu
Alloy 713C[b]	-	Bal.	13.5	-	4.2	-	-	0.10	2.0 Nb, 0.8 Ti, 6.1 Al, 0.1 Zr
IN 738[b]	-	Bal.	16.0	8.1	1.6	-	-	0.10	2.6 W, 0.8 Nb, 3.4 Ti, 3.4 Al, 1.8 Ta, 0.04 Zr
Hastelloy-X	19.2	Bal.	21.7	2.1	8.8	0.7	0.5	0.08	0.7 W
RA 333	18.0	Bal.	25.0	3.0	3.0	1.5	1.25	0.05	3.0 W
Austenitic Steels									
Type 304 SS	Bal.	9.5	19.0	-	-	2.0[c]	0.5[c]	0.08[c]	
Type 309 SS	Bal.	13.5	23.0	-	-	2.0[c]	1.0[c]	0.20[c]	
Type 310 SS	Bal.	20.5	25.0	-	-	2.0[c]	1.5[c]	0.25[c]	
Type 316 SS	Bal.	12.0	17.0	-	2.5	2.0[c]	0.5[c]	0.10[c]	
Type 321 SS	Bal.	10.5	18.0	-	-	2.0[c]	-	0.08[c]	Ti
Type 347 SS	Bal.	11.0	18.0	-	-	2.0[c]	-	0.08[c]	Nb, Ta
Incoloy 800	Bal.	32.5	21.0	-	-	1.5	1.0	0.10	0.38 Al, 0.38 Ti
HK-40[b]	Bal.	19.8	26.4	-	0.5[c]	0.6	0.8	0.38	
Ferritic Steels									
2¼Cr-1Mo	Bal.	-	2.25	-	1.0	0.5	0.5	0.15[c]	
9Cr-1Mo	Bal.	-	9.0	-	1.0	0.5	0.6	0.15[c]	
Type 446 SS	Bal.	-	25.0	-	-	1.5[c]	1.0[c]	0.20[c]	
C12[b]	Bal.	-	8.2	-	1.1	0.35	0.35	0.16	
HC[b]	Bal.	3.1	26.9	-	-	1.0	0.7	0.12	
CA-40[b]	Bal.	0.4	12.9	-	-	0.4	0.7	0.31	

[a] Wt. %.

[b] cast alloy.

[c] Maximum.

TABLE IX. Calcium-to-Sulfur Molar Ratios Required to Maintain 700 ppm SO_2 in the Dry Off-Gas[a]

Run No.	Treatment	Ca/S Molar Ratio
CT-1	None	3.4
CT-2	0.3 mol % $CaCl_2$	3.5
CT-3	0.5 mol % NaCl	3.6

[a] Experimental Conditions:

Bed Temperature - 850°C

Pressure - 101.3 kPa (1 atm)

Fluidizing Velocity - 1 m/s

Fluidized-bed Height - 513 mm

Excess O_2 - 3 % in dry off-gas

Coal - Sewickley (-12 +100 mesh), 5.46 % S

Sorbent - Grove limestone (-10 +30 mesh), 95.3 % $CaCO_3$

TABLE X. Materials, Location, and Temperature of Corrosion Specimens for Run CT-1

Corrosion-probe Designation[a]	Specimen Material[b]	Probe Location	Mean Temperature,[c] °C
		Bed Section	
C-1	Inconel 601, Inconel 671, Hastelloy-X, Type 310 SS Haynes 188, RA 333, Type 347 SS	102 mm above gas distributor plate	848
AC-2	Type 321 SS, Inconel 601, Type 310 SS, Incoloy 800, Inconel 617, RA 333, Type 309 SS	305 mm above gas distributor plate	598, 675, 724
AC-1	Type 304 SS, Type 446 SS, 2¼Cr-1Mo Steel, Incoloy 800, 9Cr-1Mo Steel, Type 316 SS, Type 309 SS	508 mm above gas distributor plate	429, 699, 727
C-2	Inconel 625, Inconel 718, Incoloy 800, Type 310 SS, Inconel 617, Type 304 SS, Type 316 SS	610 mm above gas distributor plate	844
		Freeboard Section	
C-4	Type 304 SS, Incoloy 800, Alloy 713C, Type 310 SS, IN 738, Haynes 188, Type 347 SS	394 mm above top of bed	673
AC-3[d]	Type 321 SS, Inconel 601, Type 310 SS, Incoloy 800, Inconel 617, RA 333, Type 309 SS	1003 mm above top of bed	585, 471, 630
C-3	Inconel 601, Hastelloy-X, Inconel 617, Type 310 SS, Inconel 671, Haynes 188, RA 333	1308 mm above top of bed	566

---

[a] AC = air-cooled probe; C = uncooled coupon holder.

[b] Materials listed according to stacking sequence on the probe: first specimen towards pipe bushing, last specimen near the end cap.

[c] The temperatures listed for air-cooled probes were measured in specimens of Type 321 SS, Type 304 SS, Incoloy 800, and Type 309 SS.

[d] No coolant air was required for this probe.

TABLE XI. Materials, Location, and Temperature of Corrosion Specimens for Run CT-2

Corrosion-probe Designation[a]	Specimen Material[b]	Probe Location	Mean Temperature,[c] °C
		Bed Section	
C-2	Inconel 625, Inconel 718, Incoloy 800, Type 310 SS, Inconel 617, Type 304 SS, Type 316 SS	102 mm above gas distributor plate	819
AC-2	Inconel 601, Type 321 SS, Type 310 SS, Incoloy 800, Inconel 617, RA 333, Type 309 SS	305 mm above gas distributor plate	590, 646, 681
AC-1	Type 446 SS, Type 304 SS, 2¼Cr-1Mo Steel, Incoloy 800, 9Cr-1Mo Steel, Type 316 SS, Type 309 SS	508 mm above gas distributor plate	528, 545, 599
C-1	Inconel 601, Inconel 671, Hastelloy-X, Type 310 SS, Haynes 188, RA 333, Type 347 SS	610 mm above gas distributor plate	844
		Freeboard Section	
C-4	Alloy HK-40, Alloy HC, Alloy CA-40, Alloy C-12, Alloy 713C, IN 738, Incoloy 800	394 mm above top of bed	693
AC-3[d]	Inconel 601, Type 321 SS, Type 310 SS, Incoloy 800, Inconel 617, RA 333, Type 309 SS	1003 mm above top of bed	604, 609, 604
C-3	Haynes 188, Hastelloy-X, Inconel 601, Inconel 617, Inconel 671, RA 333, Type 310 SS	1308 mm above top of bed	587

[a] AC = air-cooled probe; C = uncooled coupon holder.

[b] Materials listed according to stacking sequence on the probe: first specimen towards pipe bushing, last specimen near the end cap.

[c] The temperatures listed for air-cooled probes were measured in specimens of Type 321 SS, Type 304 SS, Incoloy 800, and Type 309 SS.

[d] No coolant air was required for this probe.

TABLE XII. Materials, Location, and Temperature of Corrosion Specimens for Run CT-3

Corrosion-probe Designation[a]	Specimen Material[b]	Probe Location	Mean Temperature,[c] °C
		<u>Bed Section</u>	
C-2	Inconel 625, Inconel 718, Incoloy 800, Type 310 SS, Inconel 617, Type 304 SS, Type 316 SS	102 mm above gas distributor plate	852
AC-1	Type 446 SS, Type 304 SS, 2¼Cr-1Mo Steel, Incoloy 800, 9Cr-1Mo Steel, Type 316 SS, Type 321 SS	305 mm above gas distributor plate	588, 631, 613
AC-2	Inconel 601, Type 321 SS, Type 310 SS, Type 304 SS, Inconel 617, RA 333, Type 309 SS	508 mm above gas distributor plate	552 596, 597
C-1	Inconel 601, Inconel 671, Hastelloy-X, Type 310 SS, Haynes 188, RA 333, Type 347 SS	610 mm above gas distributor plate	851
		<u>Freeboard Section</u>	
C-4	Alloy HK-40, Alloy HC, Alloy CA-40, Alloy C-12, Alloy 713C, IN 738, Incoloy 800	394 mm above top of bed	701
AC-3[d]	Inconel 601, Type 321 SS, Type 310 SS, Incoloy 800, Inconel 617, RA 333, Type 309 SS	1003 mm above top of bed	621, 640, 645
C-3	Haynes 188, Hastelloy-X, Inconel 601, Inconel 617, Inconel 671, RA 333, Type 310 SS	1308 mm above top of bed	605

[a] AC = air-cooled probe; C = uncooled coupon holder.

[b] Materials listed according to stacking sequence on the probe: first specimen towards pipe bushing, last specimen near the end cap.

[c] Approximate values of temperature.

[d] No coolant air was required for this probe.

TABLE XIII. Average Values of the Thickness of Surface Scale and Internal Corrosive Penetration Measured in Corrosion Coupons for Run CT-1

Specimen Holder	Material	Surface-scale thickness, µm			Corrosive Penetration, µm			Remarks
		Top	Bottom	Side	Top	Bottom	Side	
C-1	Inconel 601	1.7	2.0	2.0	5.3	5.3	4.1	Some grain-boundary attack, ∿50 µm deep
	Inconel 671	3.1	3.4	2.5	6.4	8.5	6.6	Preferential corrosive attack of one phase ∿15 µm deep
	Hastelloy-X	a	1.2	1.2	5.1	4.2	8.5	
	Type 310 SS	1.5	1.4	2.5	17.1	11.5	21.2	Internal corrosion mainly sulfides
	Haynes 188	2.0	a	1.9	9.3	8.5	9.2	
	RA 333	1.5	a	2.4	12.7	10.7	15.2	
	Type 347 SS	1.0	a	1.9	6.0	6.4	7.3	
C-2	Inconel 625	1.4	1.7	1.4	7.8	9.3	7.4	
	Inconel 718	a	3.1	2.0	5.4	5.1	5.9	
	Incoloy 800	1.7	a	2.7	11.0	21.2	8.8	
	Type 310 SS	a	a	1.6	9.1	12.9	12.7	Internal corrosion mainly sulfides
	Inconel 617	3.2	a	3.3	16.5	16.1	9.3	Some grain-boundary attack ∿40 µm deep
	Type 304 SS	3.8	1.7	3.1	20.3	11.4	11.9	
	Type 316 SS	2.7	2.9	2.7	9.1	25.0	8.5	

[a] Surface scale spalled.

TABLE XIV. Average Values of the Thickness of Surface Scale and Internal Corrosive Penetration Measured in Corrosion Coupons for Run CT-2

Specimen Holder	Material	Surface-scale Thickness, μm			Corrosive Penetration, μm			Remarks
		Top	Bottom	Side	Top	Bottom	Side	
C-1	Inconel 601	a	2.0	2.0	7.4	6.7	3.0	Some grain-boundary attack $\sim$33 μm deep
	Inconel 671	a	5.6	6.7	63.0	77.5	11.5	
	Hastelloy-X	a	a	2.0	20.7	10.7	7.3	
	Type 310 SS	1.3	a	2.0	7.6	11.0	9.8	Internal corrosion mainly sulfides
	Haynes 188	a	a	1.3	11.3	13.3	8.6	
	RA 333	2.3	a	1.7	8.5	13.5	7.6	
	Type 347 SS	a	3.0	3.4	5.3	9.7	10.2	
C-2	Inconel 625	1.3	1.3	2.1	9.8	9.1	8.8	
	Inconel 718	2.0	1.7	1.5	5.9	5.9	5.1	
	Incoloy 800	3.7	1.2	1.2	5.3	7.8	7.6	
	Type 310 SS	3.4	3.0	2.3	27.1	15.4	14.6	Internal corrosion mainly sulfides
	Inconel 617	3.3	5.3	3.3	18.7	19.5	14.4	Some grain-boundary attack $\sim$25 μm deep
	Type 304 SS	2.2	3.0	2.1	13.5	11.1	10.1	
	Type 316 SS	3.4	2.5	2.5	12.3	8.0	12.7	

[a] Surface scale spalled.

TABLE XV. Average Values of the Thickness of Surface Scale and Internal Corrosive Penetration Measured in Corrosion Coupons for Run CI-3

Specimen Holder	Material	Surface-scale Thickness, μm			Corrosive Penetration, μm			Remarks
		Top	Bottom	Side	Top	Bottom	Side	
C-1	Inconel 601	a	a	3.8	32.2	40.2	38.1	
	Inconel 671	a	7.6	6.8	51.9	97.4	80.4	
	Hastelloy-X	1.9	1.7	1.7	14.8	10.6	15.6	
	Type 310 SS	2.0	2.0	2.7	15.2	10.2	15.2	Internal corrosion mainly sulfides
	Haynes 188	1.7	a	1.2	11.8	8.5	12.3	
	RA 333	a	a	2.9	22.0	37.2	37.7	Corrosion attack in some regions ∿80 μm deep
	Type 347 SS	a	a	2.5	11.0	10.1	9.3	
C-2	Inconel 625	2.5	a	2.4	17.8	16.9	9.8	
	Inconel 718	2.5	2.4	2.0	7.1	8.5	5.8	
	Incoloy 800	a	a	3.4	22.9	19.5	24.6	
	Type 310 SS	a	a	2.9	33.9	31.3	23.7	Internal corrosion mainly sulfides
	Inconel 617	2.6	a	2.4	27.5	32.8	34.8	
	Type 304 SS	2.2	a	2.4	10.8	9.3	11.8	
	Type 316 SS	a	a	3.1	8.1	9.8	18.6	

[a] Surface scale spalled.

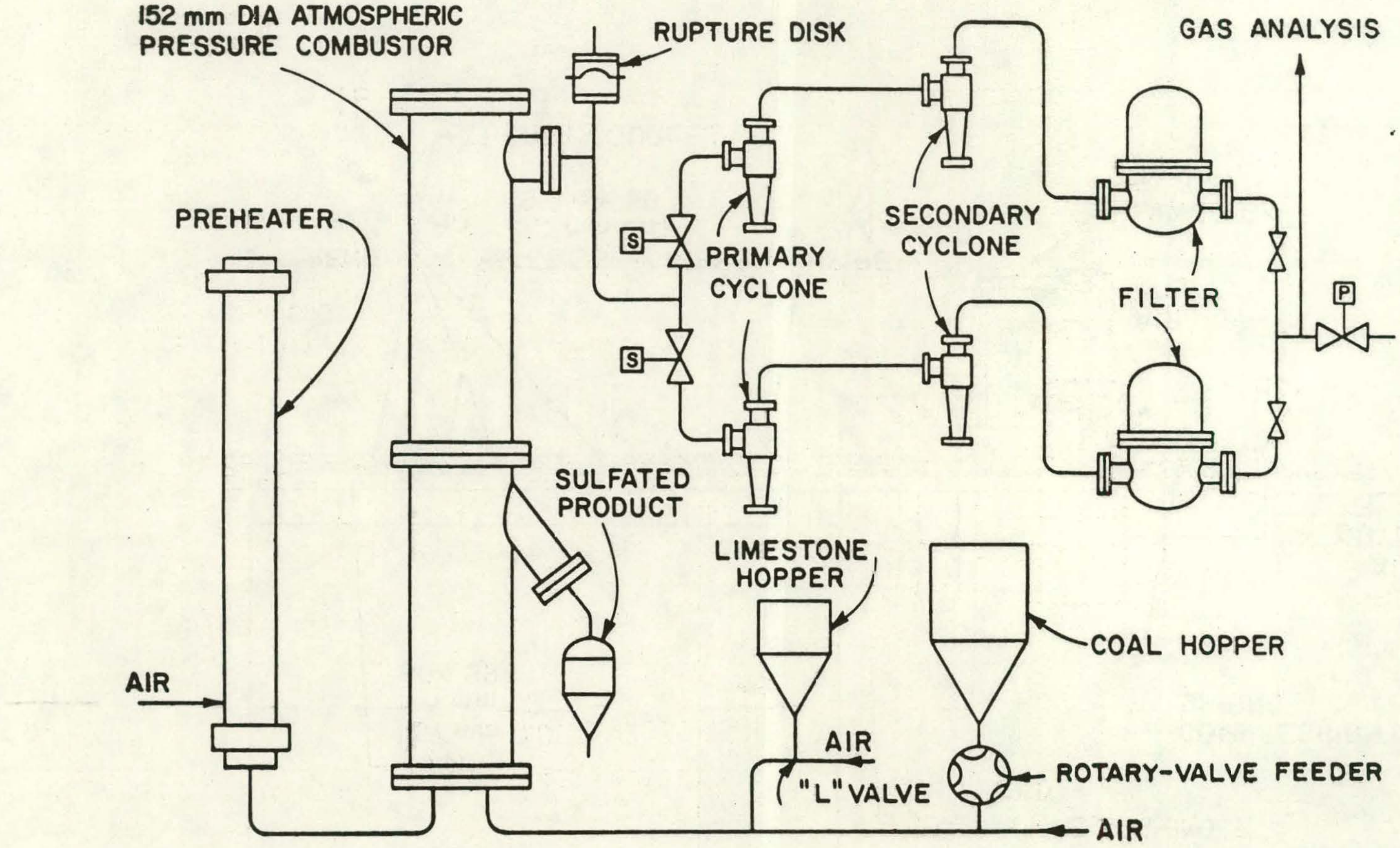

Fig. 15. Schematic Diagram of Atmospheric-pressure Fluidized-bed Combustion Test Facility. ANL Neg. No. 306-79-41R1.

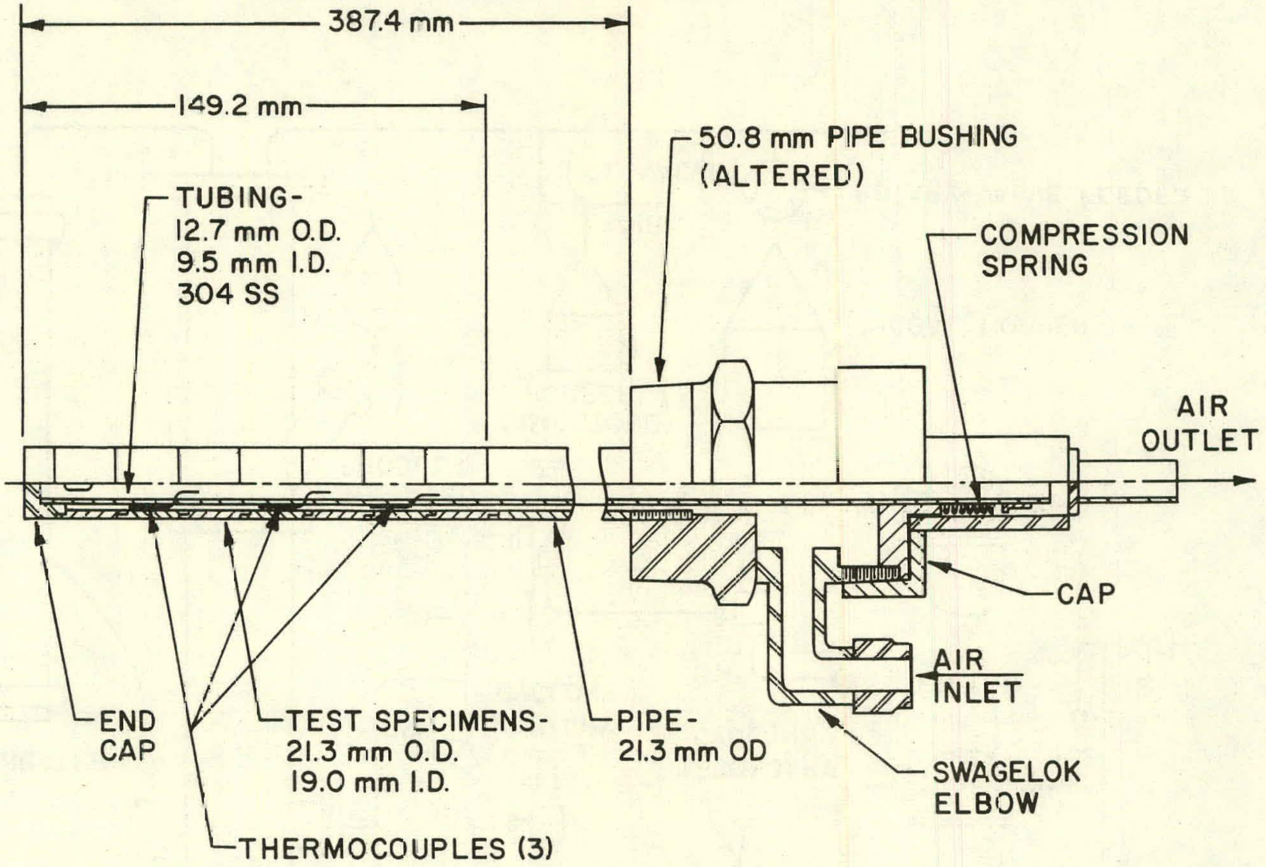

Fig. 16. Schematic of Air-cooled Corrosion Probe. ANL Neg. No. 306-79-45 R.

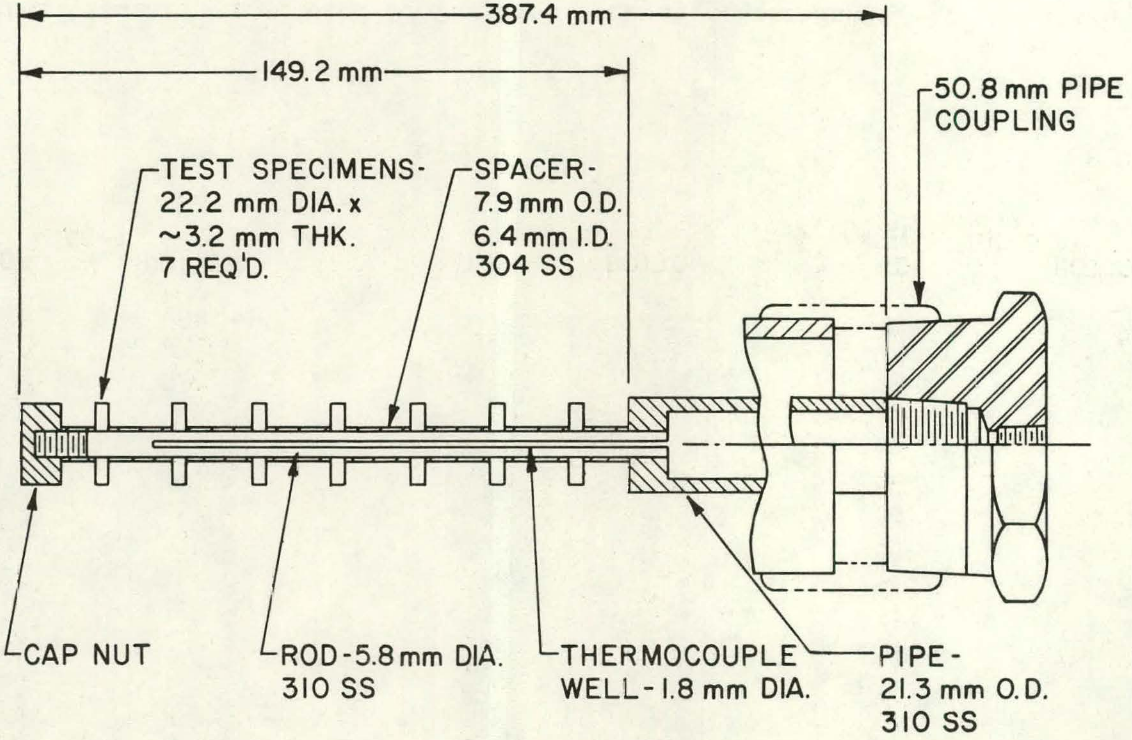

Fig. 17. Schematic of Uncooled Corrosion-coupon Holder. ANL Neg. No. 306-79-44 R.

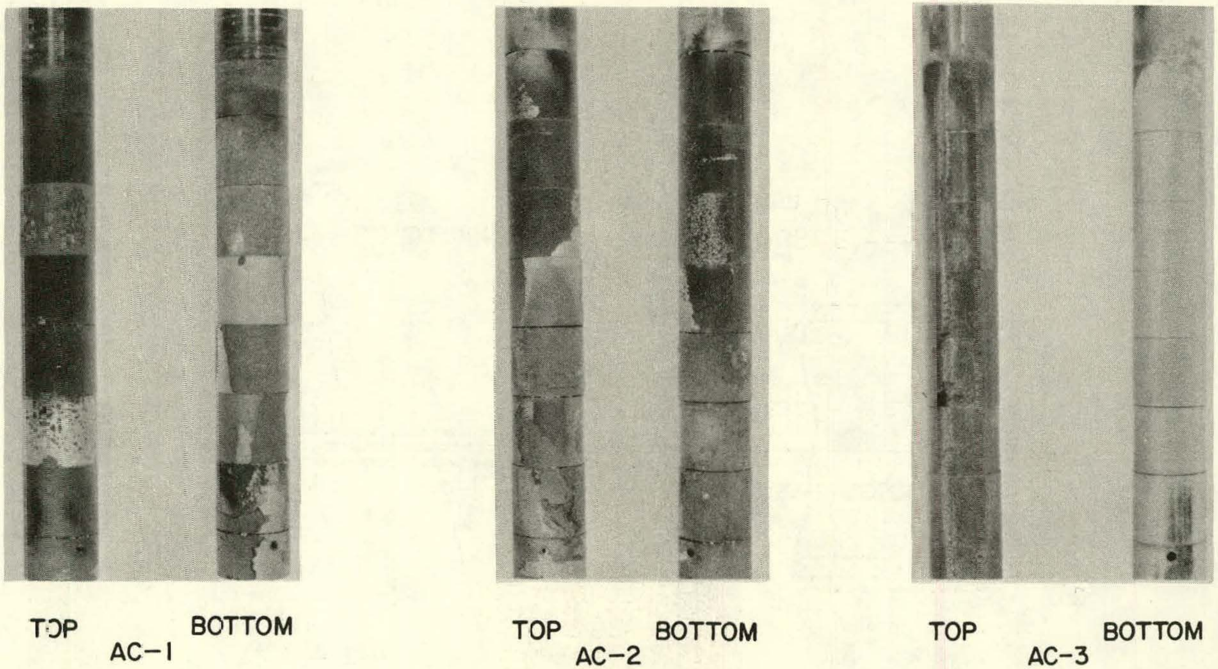

Fig. 18. Top and Bottom Views of Air-cooled Probes from Corrosion Test Run CT-1. Specimens stacked from top to bottom according to the sequence listed in Table X. ANL Neg. No. 306-79-53 R.

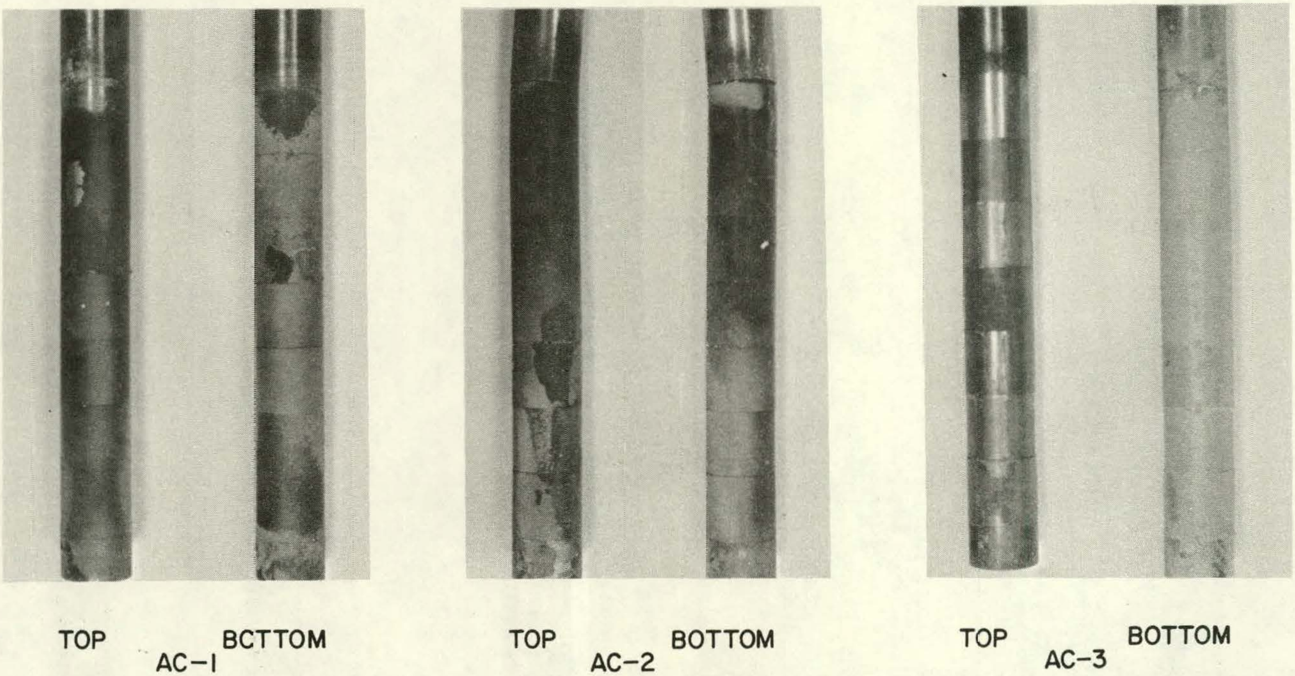

Fig. 19. Top and Bottom Views of Air-cooled Probes from Corrosion Test Run CT-2. Specimens stacked from top to bottom according to the sequence listed in Table XI. ANL Neg. No. 306-79-54 R.

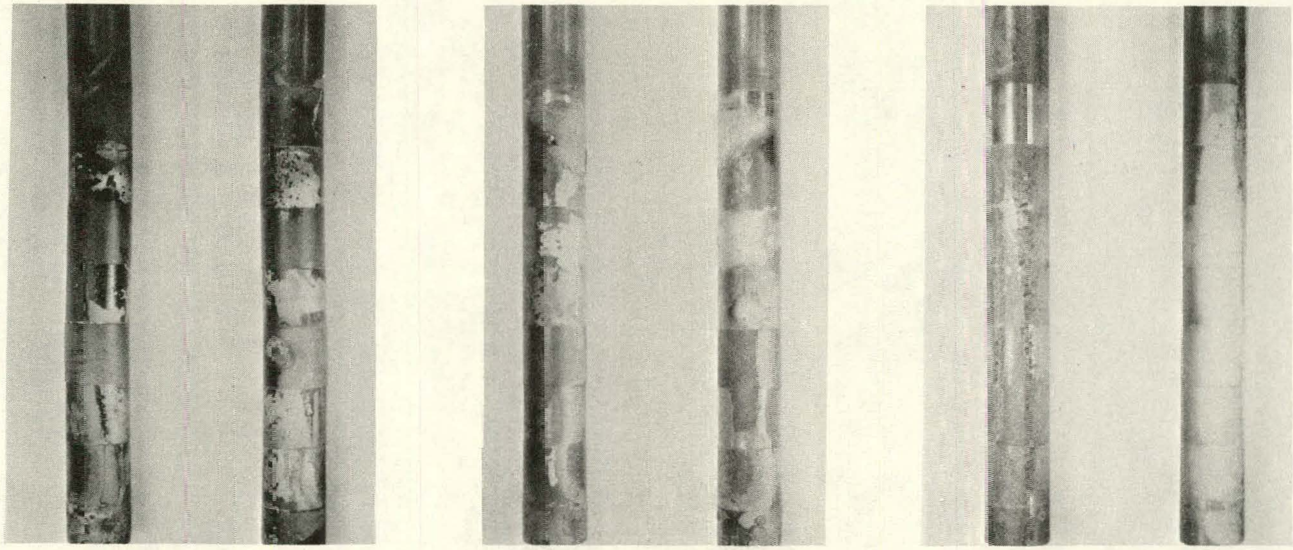

TOP AC-1 BOTTOM

TOP AC-2 BOTTOM

TOP AC-3 BOTTOM

Fig. 20. Top and Bottom Views of Air-cooled Probes from Corrosion Test Run CT-3. Specimens stacked from top to bottom according to the sequence listed in Table XII. ANL Neg. No. 306-79-52 R.

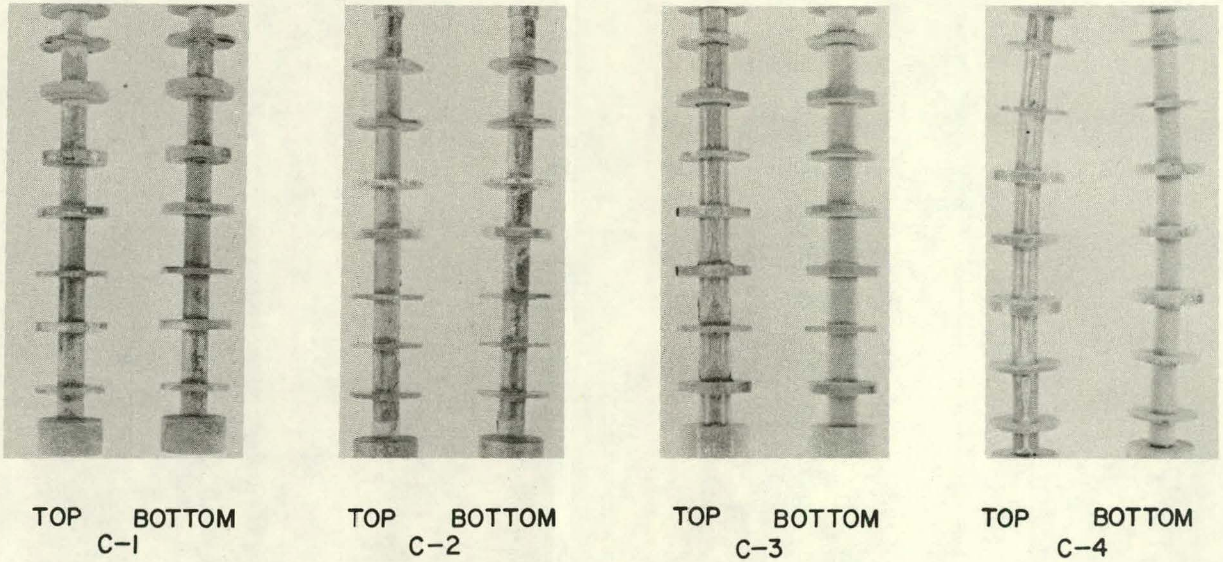

Fig. 21. Top and Bottom Views of Uncooled Coupon Holders from Corrosion Test Run CT-1. Specimens stacked from top to bottom according to the sequence listed in Table X. ANL Neg. No. 306-79-49 R.

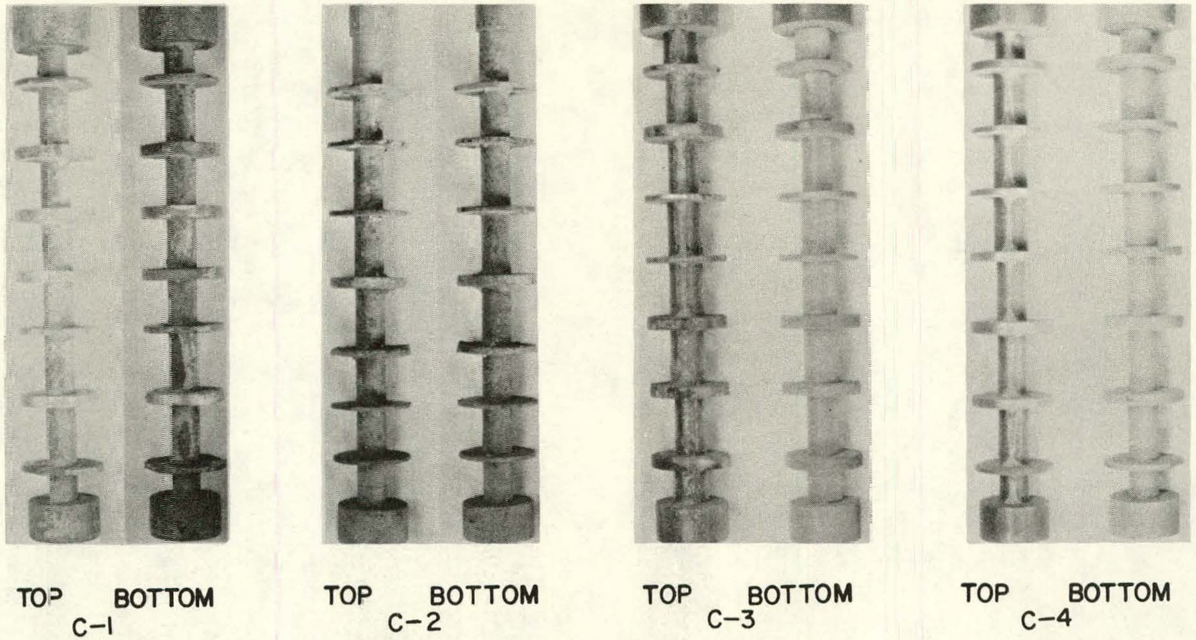

Fig. 22. Top and Bottom Views of Uncooled Coupon Holders from Corrosion Test Run CT-2. Specimens stacked from top to bottom according to the sequence listed in Table XI. ANL Neg. No. 306-79-51 R.

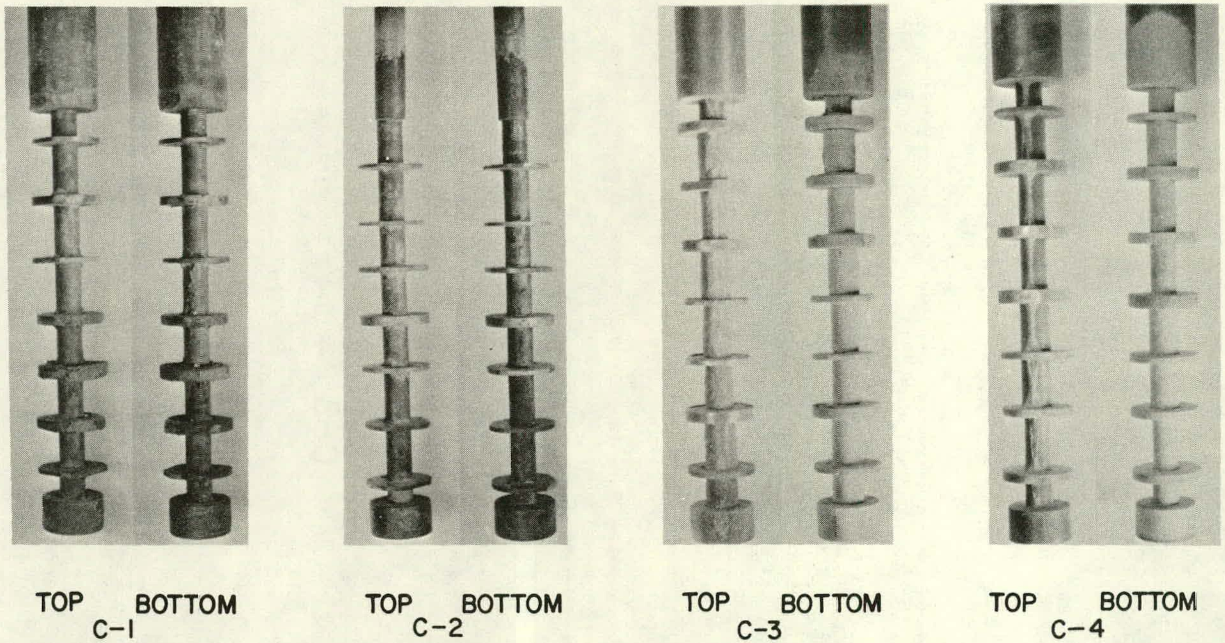

Fig. 23. Top and Bottom Views of Uncooled Coupon Holders from Corrosion Test Run CT-3. Specimens stacked from top to bottom according to the sequence listed in Table XII. ANL Neg. No. 306-79-50 R.

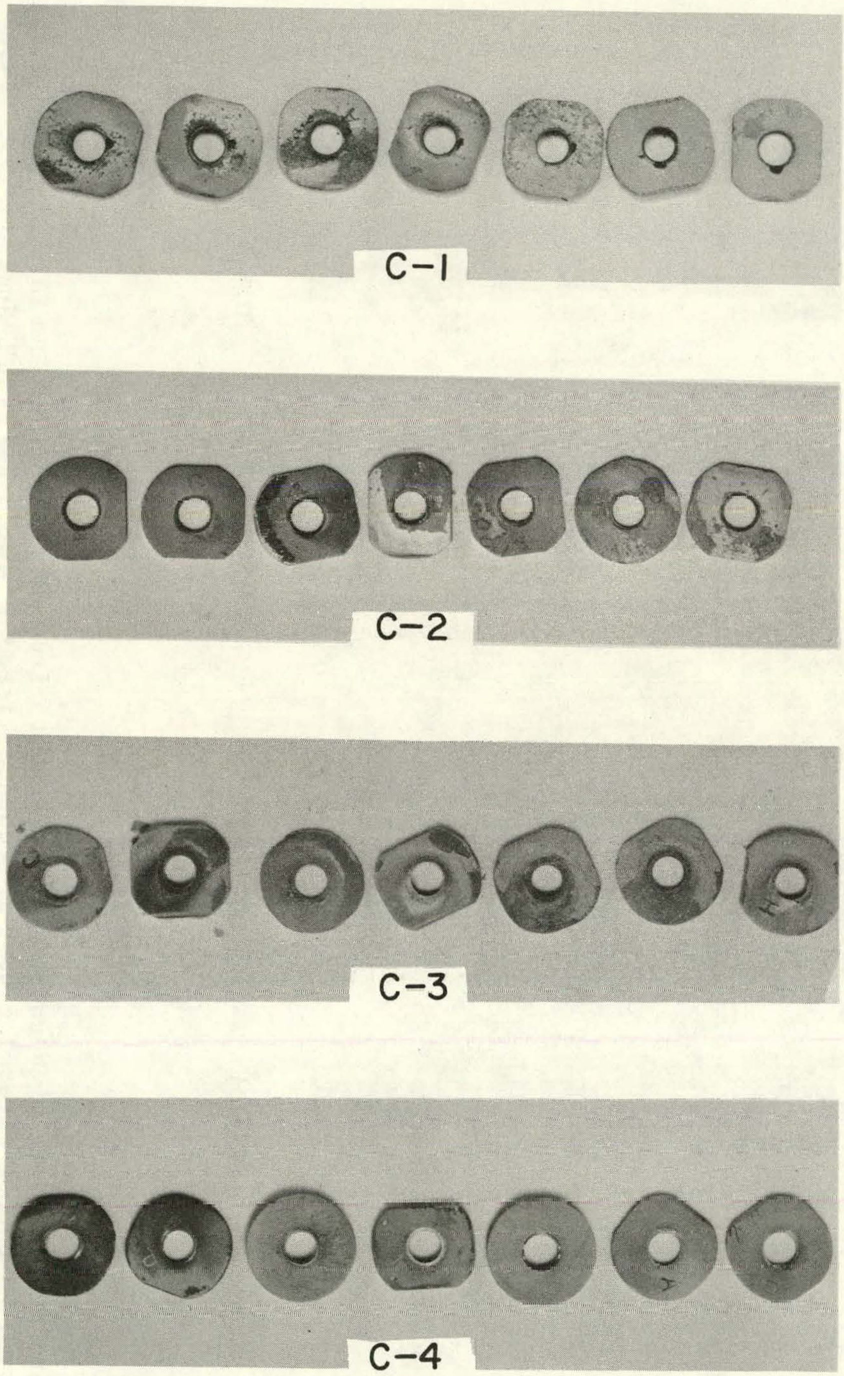

Fig. 24. Corrosion Coupons from Run CT-1. ANL Neg. No. 306-79-47.

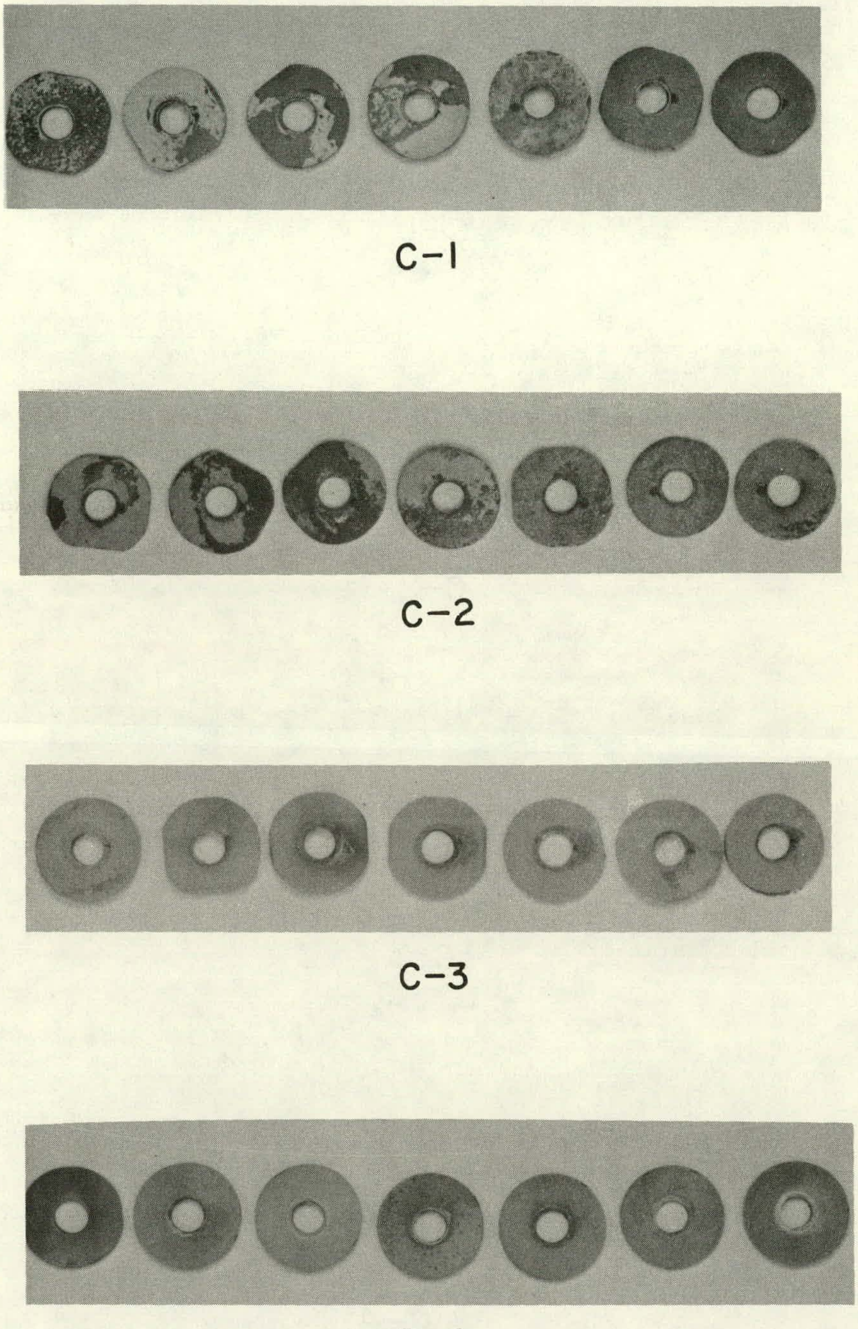

C-1

C-2

C-3

C-4

Fig. 25. Corrosion Coupons from Run CT-2. ANL Neg. No. 306-79-46.

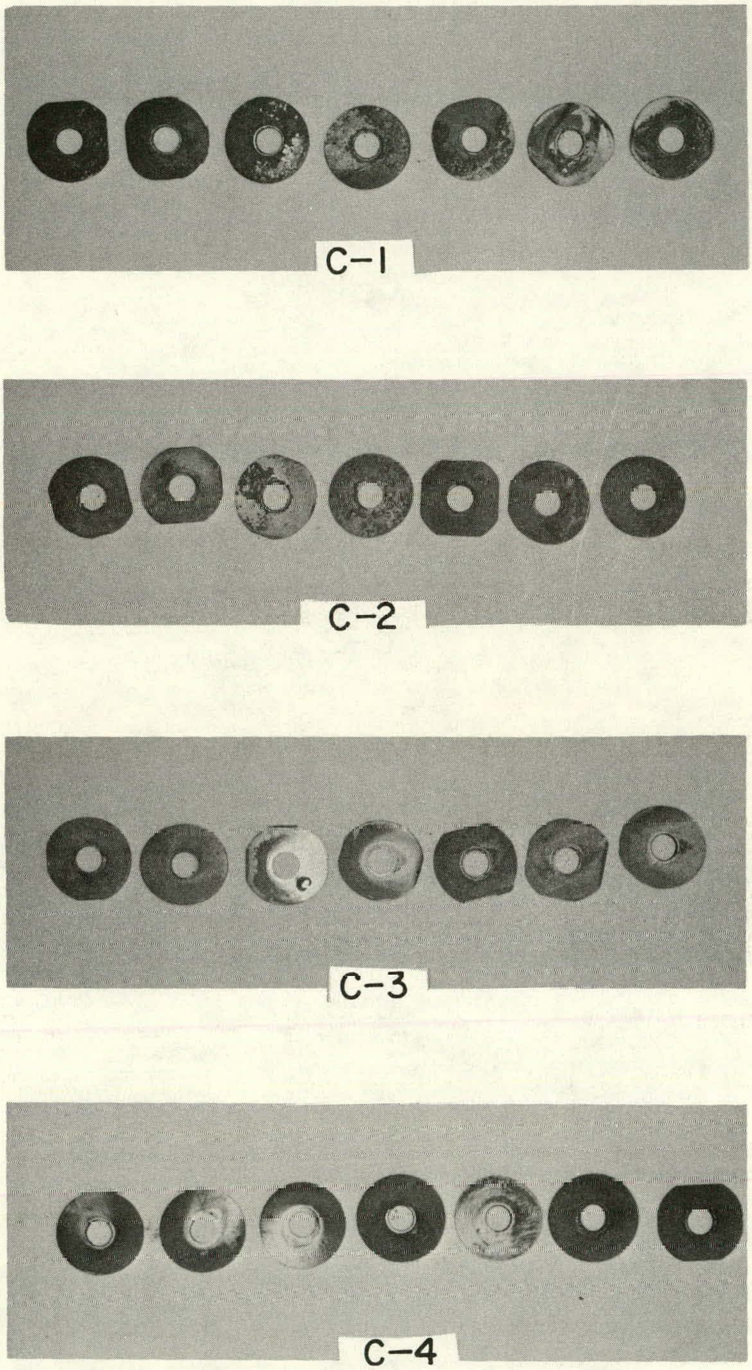

Fig. 26. Corrosion Coupons from Run CT-3. ANL Neg. No. 306-79-48.

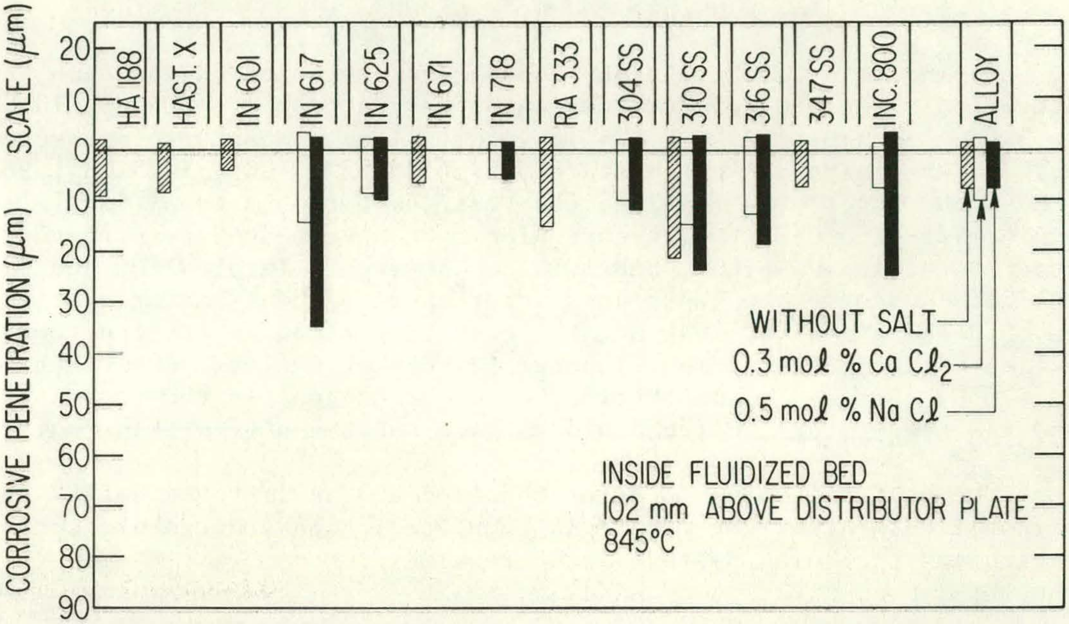

Fig. 27. Average Thickness of Surface Scale and Internal Corrosive Penetration for Corrosion Coupons Exposed Inside the Fluidized Bed for 360 ks at a Location 102 mm Above the Gas Distributor Plate. ANL Neg. No. 306-79-43R1.

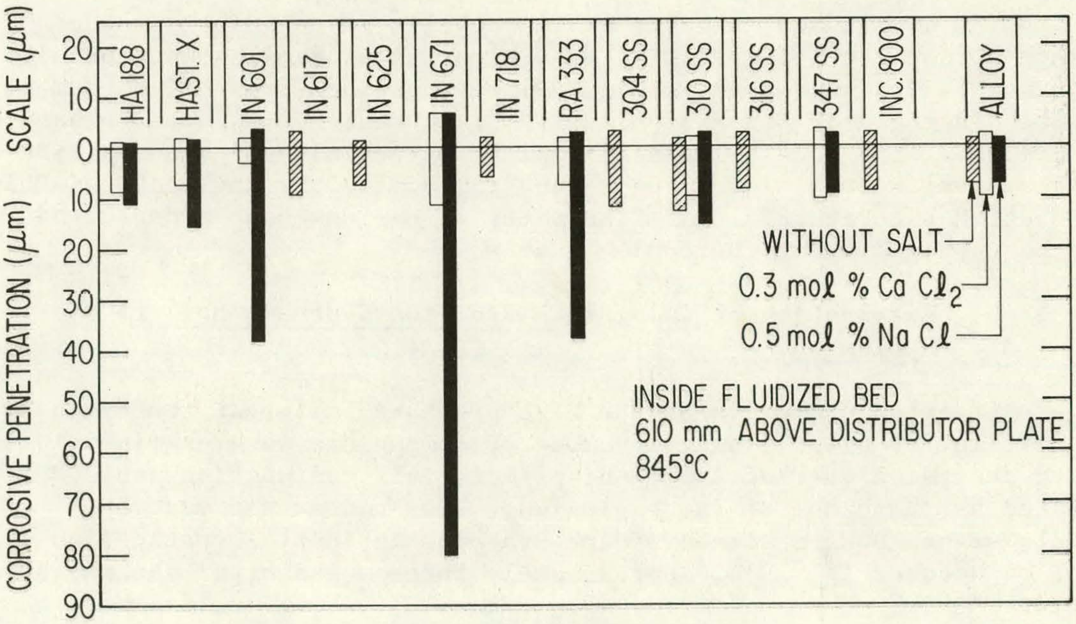

Fig. 28. Average Thickness of Surface Scale and Internal Corrosive Penetration for Corrosion Coupons Exposed Inside the Fluidized Bed for 360 Ks at a Location 610 mm Above the Gas Distributor Plate. ANL Neg. No. 306-79-42R1.

Task E -- Erosion Behavior of Materials in Coal-conversion Processes

(J.Y. Park, S. Danyluk, and W.J. Shack)

During this quarter, high-temperature corrosion calibration tests were attempted in an MPC-selected corrosion test atmosphere (24 H_2, 18 CO, 12 CO_2, 3 CH_4, 39 H_2O, 1 H_2S, 1 NH_3 in volume %) at atmospheric pressure and 816°C. Three separate gas mixtures (51.4 CO, 34.3 CO_2, 14.3 CH_3; 96 H_2, 4 H_2S; NH_3) and water were fed into the test chamber at a total flow rate of 16 ml/s (2 cfh). Twelve corrosion test specimens were prepared from Type 304 stainless steel, SAE 1015 carbon steel, Incoloy 800 and Stellite 6B. However, the tests were interrupted 32 hours after start-up because of a cooling-water leak and the resultant flood in the test chamber. At the time of the interruption, the temperature of the test chamber had reached 570°C. Because of uncertainty of water content in the test environment and low temperature, corrosion data were not taken from this run.

The test apparatus is being repaired and an improved safety shutoff system installed. After the repair is completed, high-temperature corrosion calibration and screening tests will be resumed.

Task F -- Component Performance and Failure Analysis *(S. Danyluk, G.M. Dragel and L.E. Pahis)*

a. IGT U-GAS Thermowell Exposure

The design and assembly of thermowells for exposure in the Institute of Gas Technology (IGT) U-GAS Plant is proceeding on schedule. The thermowell design (shown in Fig. 29) was obtained from Dr. M. Mamoun, IGT. The design calls for a 3/4-in. I.P.S. Schedule 40 pipe to be used as the thermowell. The sheath material will be Haynes Alloy 188 and a Type 310 stainless steel with a slurry fusion coating applied by the Lockheed Palo Alto Research Laboratories. All the material has now been ordered and should be received during the coming quarter.

b. Examination of Components from the Synthane Boiler Explosion

After an explosion of the high-pressure boiler at the Synthane coal-gasification pilot plant, a number of components were examined in order to determine whether a mechanical/materials malfunction could be pinpointed as the cause of the explosion. The request was made by Mr. Paul Neeson, DOE, Chairman of the Synthane Accident Investigation Committee, on October 11, 1978, approximately three weeks after the accident occurred.

A large number of components were examined in the investigation. The inventory of the received components is shown in Table XVI. Components A through I were disassembled and visually inspected before testing. The relays and timers (J) were not disassembled, but were tested individually using a standard checkout board.

The specific mechanical/materials malfunction which led to the explosion of the boiler could not be identified from the evaluation of the components.

Details of this investigation will be appended to the final report that will be issued by the DOE Chicago Operations Office.

c. IGT Pilot Plant - Cracks in Steam Piping from the Steam-Iron Pilot Plant

Five sections of 10.16-cm (4-in.)-diameter AISI Type 304 stainless steel pipe that had been in service for approximately two years developed leaking cracks near welds. The pipe is used to transport steam in the IGT Steam-Iron pilot plant. The gas composition at the ID of the pipe was as follows (wt. %): 0.2 CO, 2.4 CO_2, 0.1 Ar, and 0.1 CH_4. An occasional trace of H_2S was detected. The coal/char particulate loading rate was moderate to heavy. The nominal gas pressure and temperature were 3.5 MPa (500 psi) and 238°C (460°F), respectively. The cracks initiated at the ID and were of two types: Intergranular cracks, attributed to stress corrosion caused by sensitization and to residual stresses due to welding and corrosive elements in the steam, and transgranular cracks, attributed to chloride-assisted stress corrosion.

Figure 30 shows a schematic of one of these pipe sections, welded to the neck of a 6-in., 150-lb weld-neck flange. Transgranular cracks were found in the weld metal, pipe and weld neck as indicated in the figure. Intergranular cracking also occurred, at $\sim$ 1 cm from the weld fusion line. Figure 31 shows a micrograph of a cross section of the same weld neck. The major crack is intergranular, but transgranular cracks initiating at the fracture surface are also visible. This intergranular crack was responsible for the leak. The transgranular crack had propagated through only a portion of the thickness.

It was suggested that the intergranular cracking could be minimized by replacing the cracked pipe with AISI Type 316L stainless steel pipe. Since this alloy is low in carbon, carbide precipitation to the grain boundaries during welding will be minimized. Also, this alloy is known to resist chloride-assisted stress-corrosion cracking better than AISI Type 304 stainless steel.

d. Pump-shaft Failure from the HYGAS Pilot Plant

A steel pump shaft from a quench-water recirculating pump cracked near one end after about one year of intermittent service (40% duty cycle). The pump is used to circulate a 150°F water mixture containing 5% solid particles with a mesh size of 100-200. The failure occurred in cold weather after steam tracing was lost and the pump was idle for $\sim$ 1-1/2 mos. The failure was at the shaft end and occurred by shear, which was apparently due to overload and vibration resulting from eccentricity of the shaft. The fracture-surface features were obliterated by rubbing of the mating faces.

The shaft was replaced with a spare and after intermittent service, vibration was again noticed. This shaft was measured for concentricity and it was found that one end was bent 0.02 mm (0.008 in.). This deviation caused the vibration. The cause of the eccentricity is not presently known.

e. Embrittlement of Experimental Test Pipe - Heat Exchanger from the Ash-Agglomerating Gasifier

An experimental test pipe, 0.95 cm (0.4 in.) in diameter, was exposed for ∿ 150 h in the Ash-Agglomerating Gasifier environment. The gas composition (mole %) at the OD was: 8 H_2, 1 CH_4, 70.7 N_2, 12.5 CO and 7.8 CO_2. The temperature was 787-899°C (1450-1650°F). The tube transported city water.

Intergranular cracks developed at a bend in the tube. The leaking cracks initiated at the OD but severe grain-boundary embrittlement occurred at both the OD and ID. Figure 32 is a micrograph showing the intergranular nature of a crack that had penetrated ∿ 50% of the wall thickness. A corrosion scale at the grain boundaries is clearly evident.

A chemical analysis revealed that the tube is similar in composition to an Incoloy 800 and not a Type 310 Stainless Steel as presumed by IGT personnel.

Electron microprobe and SEM investigations are continuing to deduce the chemistry of the corrosion scale.

f. Intergranular Stress-corrosion Cracking of Incoloy 800 Piping - HYGAS Quench-separator Enclosure

An Incoloy 800 pipe, 10.2 cm in diameter, used in the quench-separator float enclosure at the HYGAS pilot plant, developed a leaking crack near a weld. The pipe had been in service for about one year. The pipe carries a mixture of toluene and water (204°C; 6.9 MPa) from the quench tower to the quench-separator vessel.

The leak resulted from an intergranular crack that originated at the ID of the pipe, ∿ 0.6 cm from the weld fusion line. Figure 33 shows a schematic of the pipe and section removed for metallography (a), an as-polished cross section showing the ID, OD, crack and weld (b), an etched cross section with the weld, OD and intergranular crack (c), and the etched cross section with the weld, ID and intergranular crack (d).

The failure is attributed to intergranular stress-corrosion cracking resulting from sensitization and residual stresses that are imposed during welding and noxious elements in the toluene and water mixture.

g. Erosion of a Carbon Steel Pipe from the Westinghouse Coal-gasification PDU

An ASTM A106 Gr.B. Schedule 40 carbon steel pipe, 2.54 cm in diameter, failed as a result of erosion after ∿ 30 months of service (30% duty cycle). The failure was noticed after the pipe had been exposed to a flow of recycle gas for 20 months, and a smaller transport tube was mounted concentrically to perform the same function. The failure occurred near a weld to a 310 stainless steel C115 gasifier vessel. The operating temperature was ∿ 316°C (∿ 600°F).

A section of the failed pipe was examined at ANL to confirm the failure mechanism and investigate possible generic erosion problems.

A photograph of the ID surface of the failed tube is shown in Fig. 34. The surface appears mottled with deep gouges and grooves. A cross-sectional view of the most eroded section is shown in Fig. 35. The thickness of the cross section was reduced by at least 50%.

SEM micrographs of the ID surface are shown in Fig. 36. Besides the corrosion scale, classic solid-particle erosion by plowing is evident. This behavior was expected and can be predicted by the Finnie method.[15]

TABLE XVI. Inventory of Received Components

A. Cashco Differential Pressure Valve (PDCV 3313)
B. Honeywell Differential Pressure Controller (PDSL 3316x)
C. Maxon Main Fuel Oil Shut-off Valve (EV354x)
D. Asco Pilot Fuel Solenoid Valve (EV353x)
E. Atomizing Steam Solenoid Valve (EV351)
F. Republic Purge Air Flow Switch (PAF)
G. Honewell "Purple Peeper" Flame Detector (XA301)
H. IIT Fuel-oil Return Solenoid Valve (XCV350)
I. Honeywell Flame Scanner Amplifier (FPR)
J. Relays and Timers

Potter and Bromfield

Auxiliary Ignition Relay (AIR)
Combustion Air Flow Relay (CAFR)
Combustion Control Relay (CCR)
Flame Failure Relay (FFR)
Gas Limit Relay (GR)
High Gas Pressure Relay (HGPR)
High Oil Pressure Relay (HOPR)
High Steam Pressure Relay (HSPR)
Low Atomizing Steam Pressure Relay (LASPR)
Los Gas Pressure Relay (LGPR)
Low Oil Pressure Relay (LOPR)
Mater Trip Relay (MTR)
Oil Limit Relay (OR)
Purge Complete Relay (PCR)

Agastat

Burner Time Delay Relay (BTDE)
Fan Time Delay Relay (FNTDD)
Ignition Time Delay Relay (ITDE)
Purge Time Delay Relay (PTDE)
Air-steam Delay Relay (OSDR)
Time Delay Relay Model (7012AE)

Warrick

Low Water Alarm Relay (LWAR)
High Water Alarm Relay (HWAR)
Low Water Cutout Relay (LWCR)

Dunco

Control Relay (BIXBX)

Westinghouse

Control Relay (AR440A)

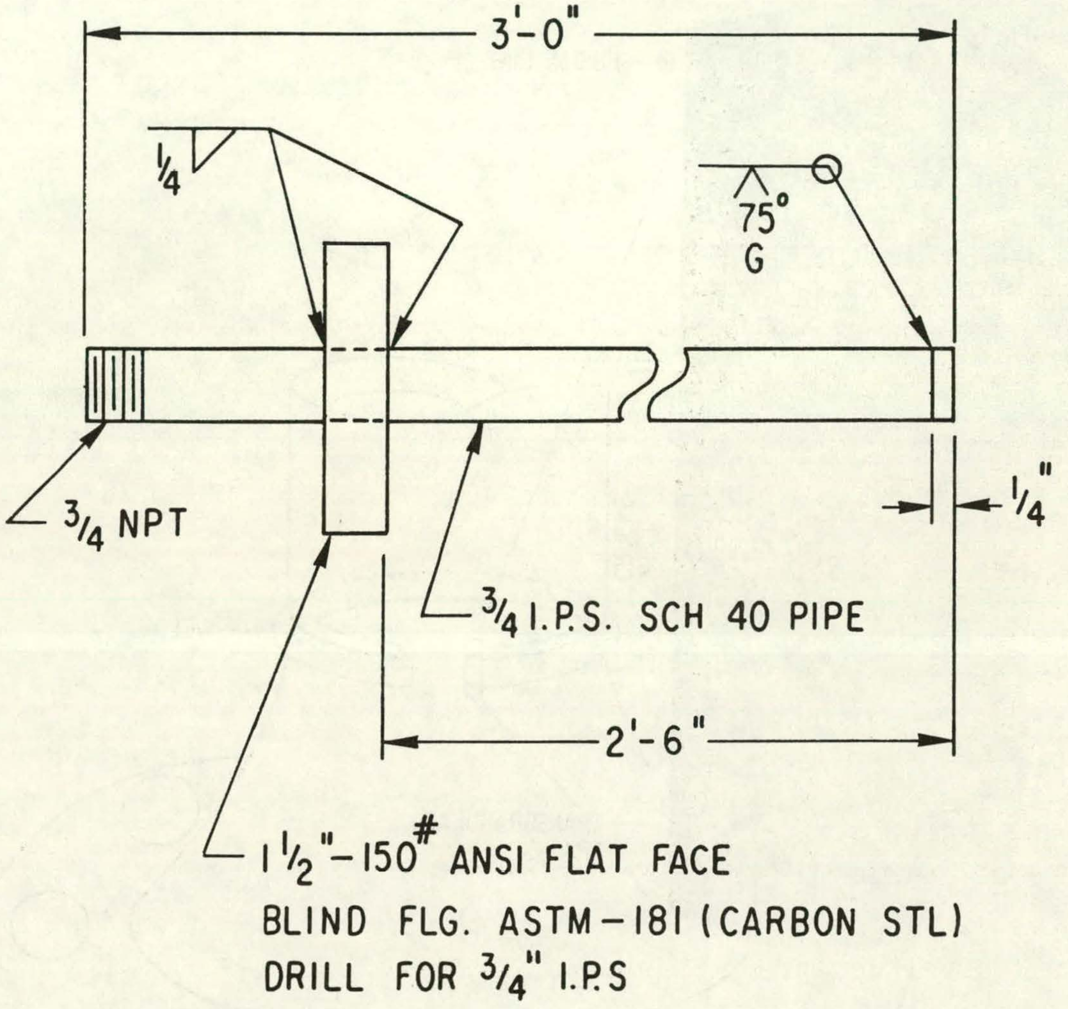

Fig. 29. Thermowell Design for the HYGAS U-Gas Exposure Tests. ANL Neg. No. 306-79-270.

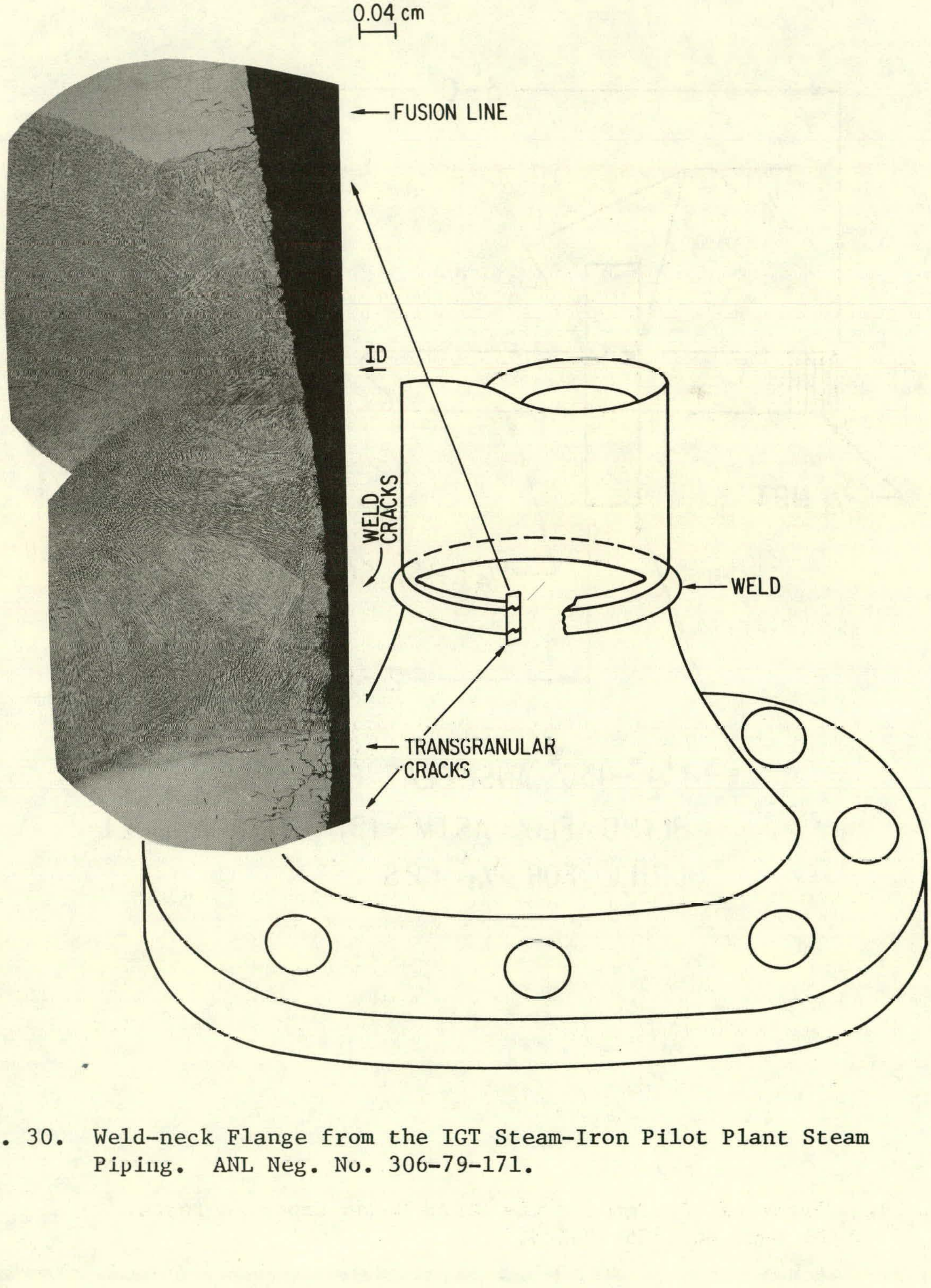

Fig. 30. Weld-neck Flange from the IGT Steam-Iron Pilot Plant Steam Piping. ANL Neg. No. 306-79-171.

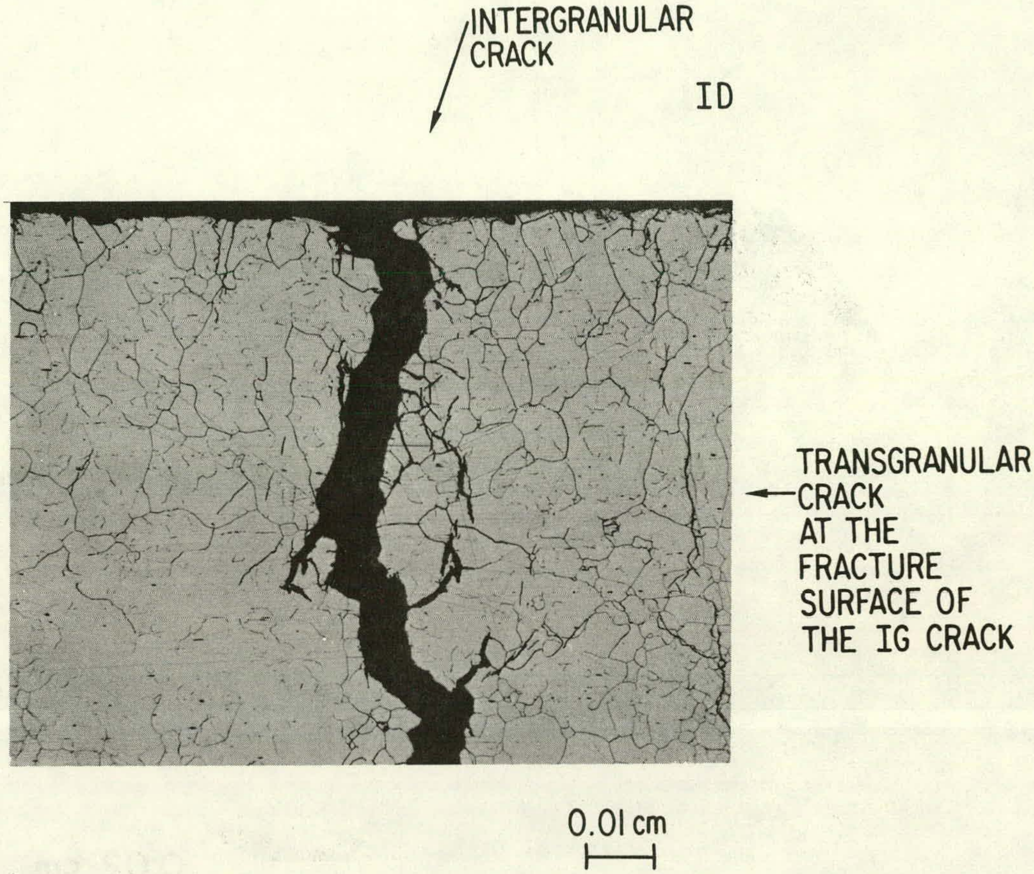

Fig. 31. Cross-sectional View of a Weld-neck Intergranular Crack. Transgranular cracks are also seen at the fracture surface of the intergranular crack. ANL Neg. No. 306-79-172.

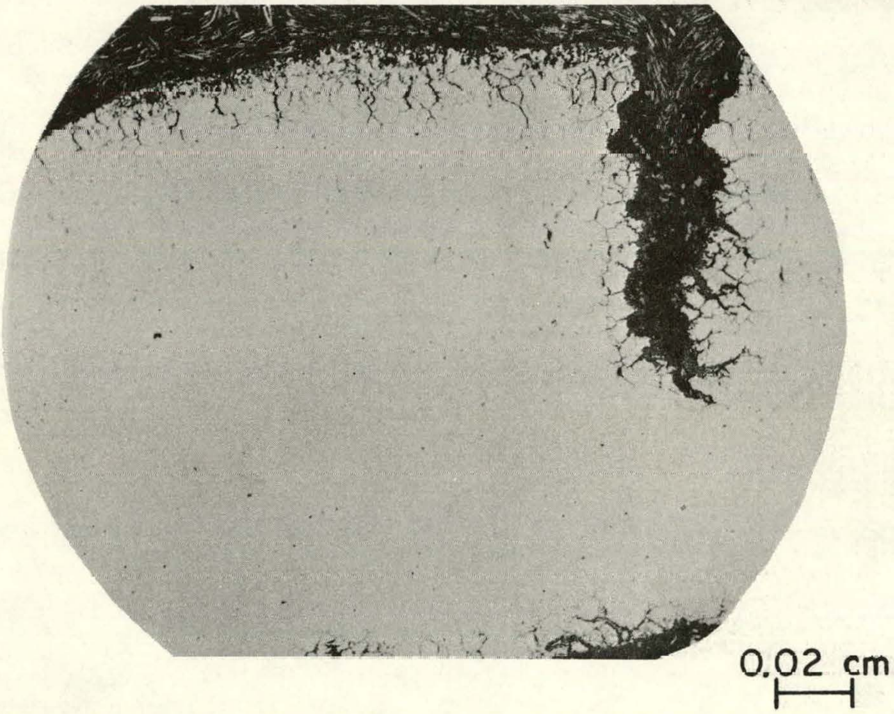

Fig. 32. Intergranular Crack and Embrittlement in the Experimental Heat-exchanger Tube. This crack initiated at the OD and propagated through ∿ 50% of the wall thickness. Embrittlement is seen at both the OD and ID. ANL Neg. No. 306-79-210.

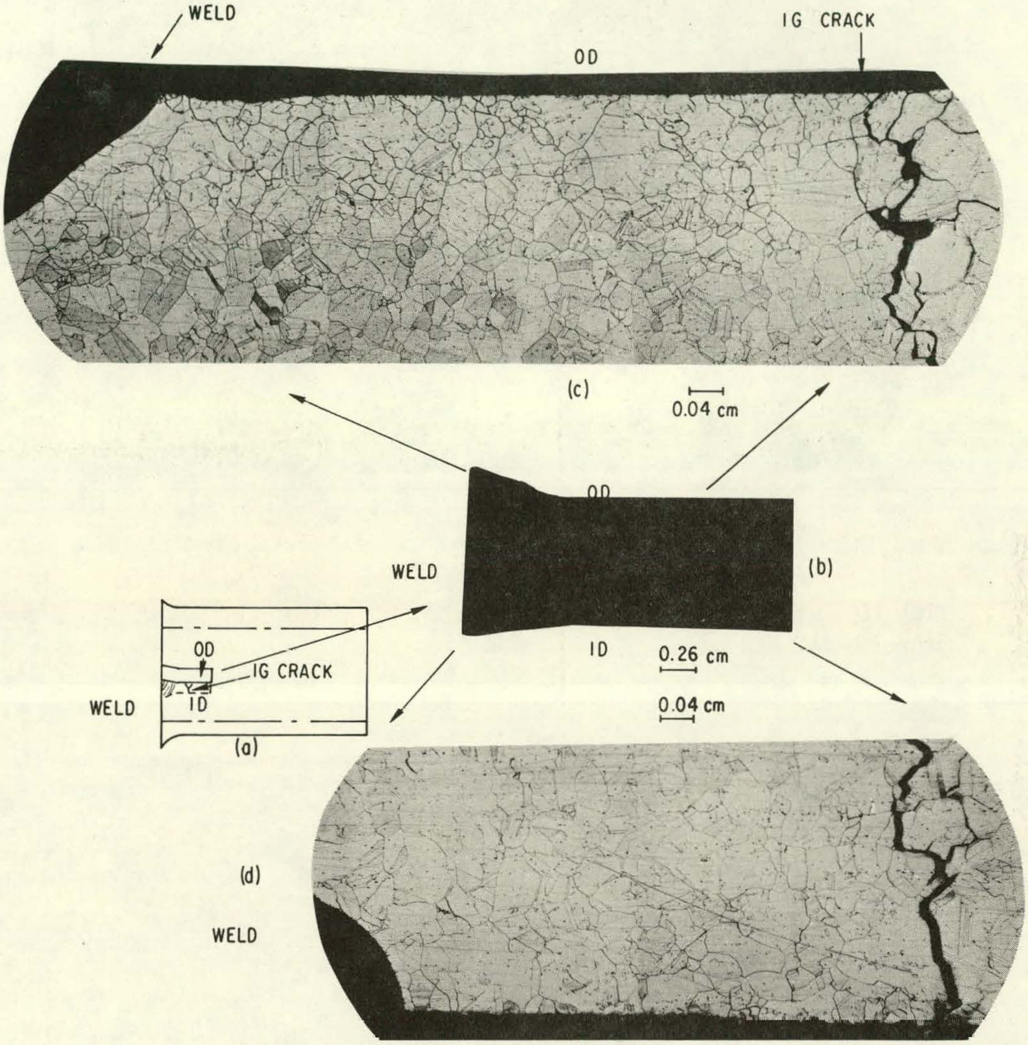

Fig. 33. Intergranular Stress-corrosion Crack from the HYGAS Quench-separator Enclosure. (a) Schematic of the Incoloy 800 pipe; (b) a polished cross section; (c) and (d) etched ID and OD cross sections. The crack originated at the ID. ANL Neg. No. 306-79-269.

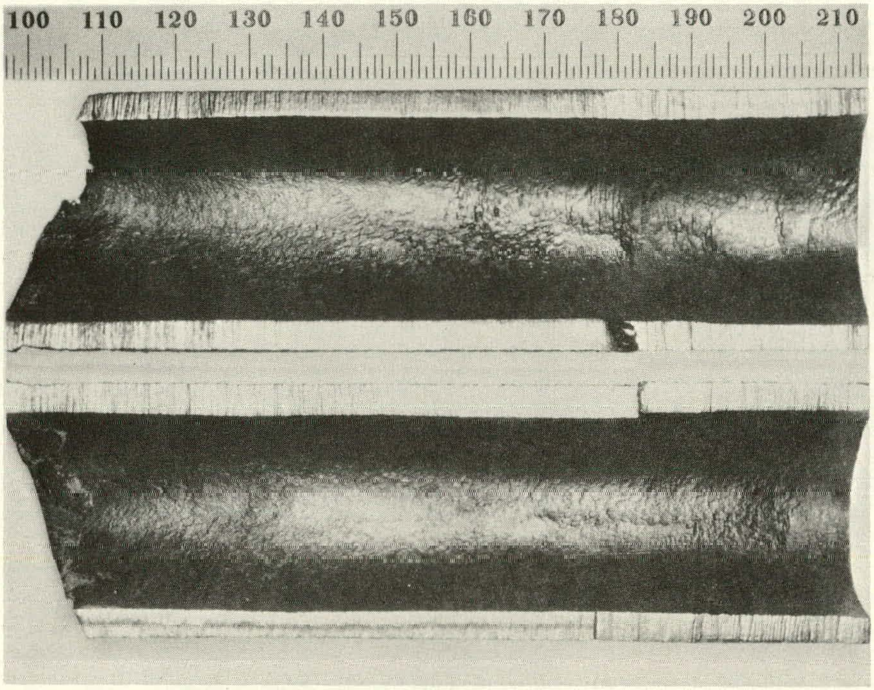

Fig. 34. The ID Surface of an Eroded Carbon Steel Pipe. ANL Neg. No. 306-79-212.

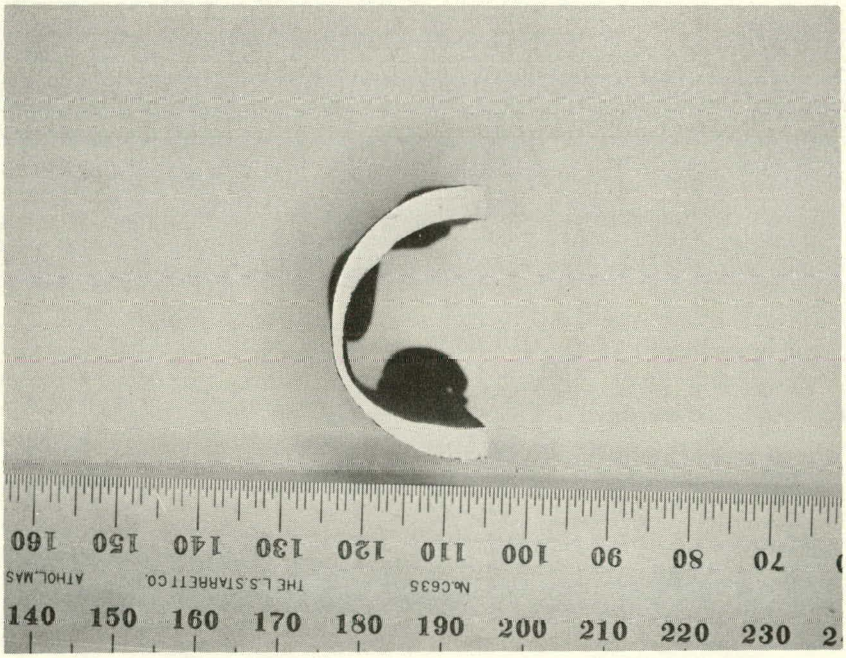

Fig. 35. Cross-sectional View of the Eroded Carbon Steel Pipe. ANL Neg. No. 306-79-211.

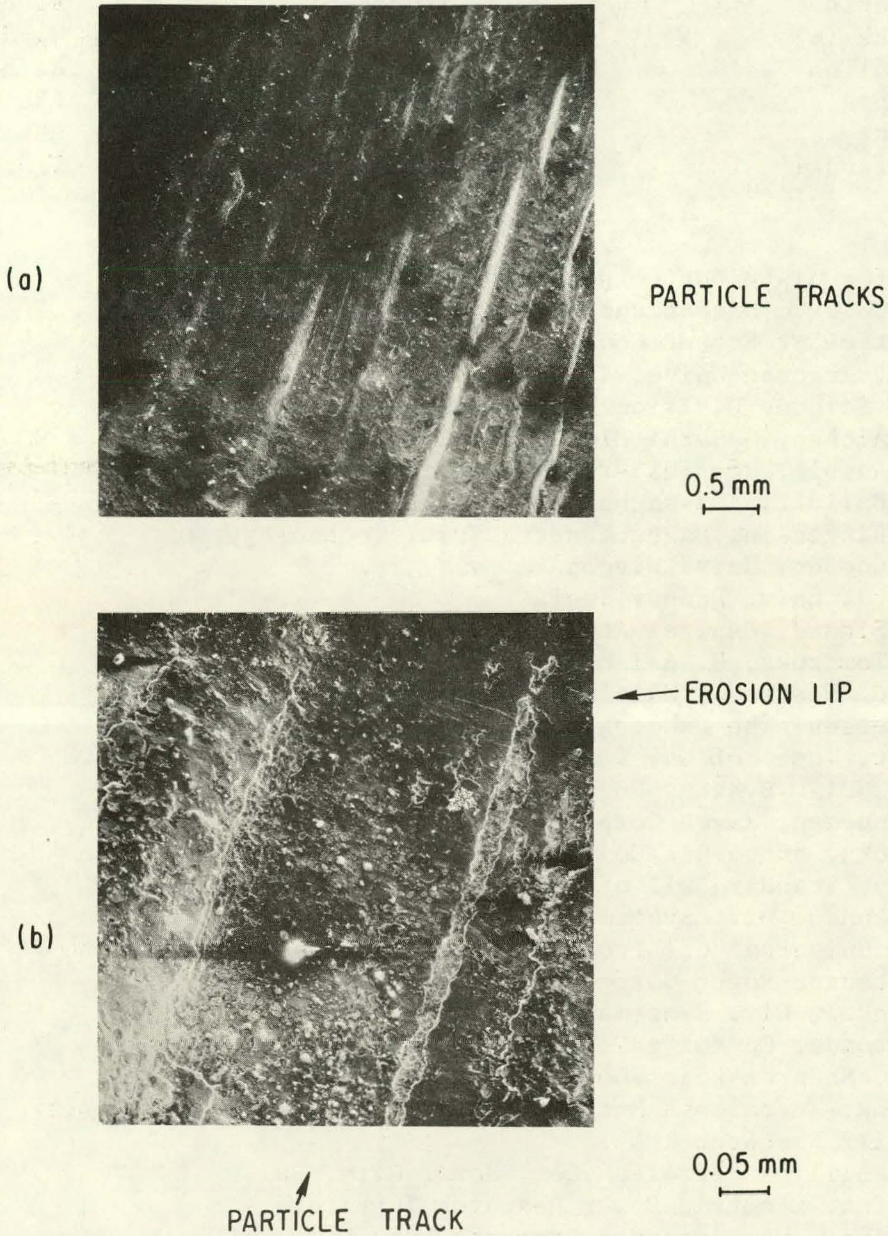

Fig. 36. Scanning Electron Micrographs of the ID Surface of the Eroded Carbon Steel Pipe. Particle tracks are readily visible in (a) and a particle track and erosion lip are seen in (b), which is an enlargement from (a). ANL Neg. No. 306-79-271.

Distribution for ANL-79-23

Internal:

E. G. Pewitt
B. R. T. Frost
J. J. Roberts
R. W. Weeks (6)
N. M. O'Fallon
O. K. Chopra
S. Danyluk
E. L. Stefanski
W. A. Ellingson (6)
K. J. Reimann
C. A. Youngdahl
A. A. Jonke
T. F. Kassner
C. R. Kennedy
K. Natesan
E. L. Hartig
J. Y. Park
R. B. Poeppel
W. J. Shack
A. B. Krisciunas
ANL Contract File
ANL Libraries (5)
TIS Files (6)

External:

DOE-TIC, for distribution per UC-90c, -90e, -90h (332)
Manager, Chicago Operations and Regional Office, DOE
Chief, Office of Patent Counsel, DOE-CORO
President, Argonne Universities Association
Materials Science Division Review Committee:
  E. A. Aitken, General Electric Co., Sunnyvale
  G. S. Ansell, Rensselaer Polytechnic Inst.
  R. W. Balluffi, Massachusetts Inst. Technology
  R. J. Birgeneau, Massachusetts Inst. Technology
  S. L. Cooper, Univ. Wisconsin
  C. Laird, Univ. Pennsylvania
  M. T. Simnad, General Atomic
  C. T. Tomizuka, U. Arizona
  A. R. C. Westwood, Martin Marietta Laboratories
E. M. Anderson, The Babcock and Wilcox Company
W. G. Bair, Inst. of Gas Technology
W. Bakker, Div. Systems Engineering, USDOE
G. B. Brenneman, Maxon Corp., Muncie, Ind.
J. A. Brooks, Amoco Oil Co., Naperville, Ill.
M. Crowley, Standard Oil of Indiana, Naperville, Ill.
S. J. Dapkunas, Div. Systems Engineering, USDOE
J. Flagg, Universal Oil Products Co., Des Plaines, Ill.
E. Fox, Stearns-Roger Corp., Homer City, Pa.
H. E. Frankel, Div. Systems Engineering, USDOE
S. M. Gaitonde, Commonwealth Edison Co., Maywood, Ill.
D. Glaser, Stearns-Roger Corp., Denver
H. Heysteck, Tuscaloosa Metallurgy Research Center, University, Ala.
V. Hill, IIT Research Inst.
D. Hull, Phillips Petroleum Co., Homer City, Pa.
R. I. Jaffee, Electric Power Research Institute
D. L. Keairns, Westinghouse Research Labs.
H. Leavenworth, Albany Metallurgy Research Center
A. V. Levey, Lawrence Berkeley Laboratory
R. Lewis, Synthane Pilot Plant, USDOE/FE, Pittsburgh
G. Long, Northern Illinois Gas Co., Aurora
R. M. Lundberg, Commonwealth Edison Co., Chicago
M. M. Mamoun, Inst. Gas Technology, Chicago
J. M. O'Donnell, The Lummus Co., Bloomfield, N.J.
A. L. Plumley, Combustion Engineering Power Systems, Windsor
J. Pope, Science Applications, Inc.

F. A. Prange, Phillips Petroleum Corp., Bartlesville
A. Sagüés, Kentucky Center for Energy, Lexington
A. Schaeffer, Metals Properties Council, New York
S. J. Schneider, National Bureau of Standards (2)
R. Searles, Ashland Synthetic Fuels, Inc., Ashland, Ky.
G. Sorrell, Exxon Research and Engineering Co., Florham Park
J. Stevenson, Rolla Metallurgy Research Center
J. Sudbury, Consolidated Coal Co., Library, Pa.
C. Whitten, Peabody Coal Co., Columbia, Tenn.

REFERENCES

1. Materials Technology for Coal-conversion Processes, Thirteenth Quarterly Report, January-March 1978, Argonne National Laboratory, ANL-78-54.

2. Materials Technology for Coal-conversion Processes, Fifteenth Quarterly Report, July-September 1978, Argonne National Laboratory, ANL-79-2.

3. Materials Technology for Coal-conversion Processes, Fourteenth Quarterly Report, April-June 1978, Argonne National Laboratory, ANL-78-79.

4. L. Pahis and S. Danyluk, ANL, Personal communication (11/10/78).

5. H.L. Dunegan, High Temperature Dynamic Modulus Measurements by Use of Ultrasonics, Mater. Eval. 22 (6), 266-276 (1964).

6. R.G. Hornbeck, METC, personal communications 10/18/78 and 1/22/79.

7. Materials Science Division Coal Technology Ninth Quarterly Report, October-December 1976, Argonne National Laboratory, ANL-77-5.

8. R.A. Perskins and M.S. Bhat, Sulfidation-Resistant Alloy for Coal Gasification Service, Lockheed Palo Alto Research Laboratories, Palo Alto, CA, FE-2299-12 (June 1977).

9. V.L. Hill and B.A. Humphreys, A Program to Discover Materials Suitable for Service Under Hostile Conditions Obtained in Equipment for the Gasification of Coal and Other Solid Fuels, Metals Properties Council Report, FE-1784-45, ed. A.O. Schaefer (November 1978).

10. D.R. Adolphson, Formation of Protective Layers on Alloys in Coal Processing Environments, Sandia Laboratories Energy Report, SAND-77-8260 (July 1977).

11. O.K. Chopra and K. Natesan, Corrosion Behavior of Type 310 Stainless Steel in Coal-Gasification Environments, Proc. Conf. on Environmental Degradation of Engineering Materials, Blacksburg, VA, Oct. 1977, M.R. Louthan and R.P. McNitt, Eds., pp. 247-256.

12. K. Natesan and M. Delaplane, Argonne National Laboratory, to be published.

13. J.A. Shearer, I. Johnson, and C.B. Turner, The Effect of Sodium Chloride on the Reaction of SO_2/O_2 Mixtures with Limestones and Dolomites, Argonne National Laboratory, ANL/CEN/FE-78-8 (1978).

14. G.J. Vogel et al., Regeneration of Sulfated Limestone from FBC's and Corrosive Effects of Sulfation Accelerators in FBC's, Annual Report July 1, 1977 - June 30, 1978, ANL/CEN/FE-78-13.

15. I. Finnie, J. Wolak and Y. Kabil, The Mechanism of Erosion of Ductile Materials, Proceedings of the 3rd National Congress of Applied Mechanics, American Society of Mechanical Engineers, pp. 527-532 (1958).